JBC RESEARCH ARTICLE

A crystallin mutant cataract with mineral deposits

Received for publication, November 1, 2022, and in revised form, June 7, 2023 Published, Papers in Press, June 17, 2023,
https://doi.org/10.1016/j.jbc.2023.104935

Peter J. Minogue[1], Junyuan Gao[2], Richard T. Mathias[2], James C. Williams Jr[3], Sharon B. Bledsoe[3], Andre J. Sommer[4], Eric C. Beyer[1,‡], and Viviana M. Berthoud[1,*,‡]

From the [1]Department of Pediatrics, University of Chicago, Chicago, Illinois, USA; [2]Department of Physiology and Biophysics, Stony Brook University, Stony Brook, New York, USA; [3]Department of Anatomy, Cell Biology and Physiology, Indiana University School of Medicine, Indianapolis, Indiana, USA; [4]Molecular Microspectroscopy Laboratory, Department of Chemistry and Biochemistry, Miami University, Oxford, Ohio, USA

Reviewed by members of the JBC Editorial Board. Edited by Phyllis Hanson

Connexin mutant mice develop cataracts containing calcium precipitates. To test whether pathologic mineralization is a general mechanism contributing to the disease, we characterized the lenses from a nonconnexin mutant mouse cataract model. By cosegregation of the phenotype with a satellite marker and genomic sequencing, we identified the mutant as a 5-bp duplication in the γC-crystallin gene (*Crygc^{dup}*). Homozygous mice developed severe cataracts early, and heterozygous animals developed small cataracts later in life. Immunoblotting studies showed that the mutant lenses contained decreased levels of crystallins, connexin46, and connexin50 but increased levels of resident proteins of the nucleus, endoplasmic reticulum, and mitochondria. The reductions in fiber cell connexins were associated with a scarcity of gap junction punctae as detected by immunofluorescence and significant reductions in gap junction-mediated coupling between fiber cells in *Crygc^{dup}* lenses. Particles that stained with the calcium deposit dye, Alizarin red, were abundant in the insoluble fraction from homozygous lenses but nearly absent in wild-type and heterozygous lens preparations. Whole-mount homozygous lenses were stained with Alizarin red in the cataract region. Mineralized material with a regional distribution similar to the cataract was detected in homozygous lenses (but not wild-type lenses) by micro-computed tomography. Attenuated total internal reflection Fourier-transform infrared microspectroscopy identified the mineral as apatite. These results are consistent with previous findings that loss of lens fiber cell gap junctional coupling leads to the formation of calcium precipitates. They also support the hypothesis that pathologic mineralization contributes to the formation of cataracts of different etiologies.

Crystallins are the major soluble proteins in the lens, accounting for about 90% of the total proteins in the organ. Lens crystallins contribute to the establishment and maintenance of the gradient of refractive index and have additional roles in development, stress responses, and chaperone activity (reviewed in (1, 2)). Cataracts are opacities within the lens that are the most frequent cause of blindness worldwide (3). They have been associated with the accumulation of modifications in the crystallins (including oxidation, deamidation, cross-linking, cleavage, fragmentation, and glycation) and the formation of insoluble high-molecular-weight protein aggregates (reviewed in (4, 5)). Several crystallin mutations have been linked to cataracts in humans and rodents (see the Cat-Map website (cat-map.wustl.edu) for an updated list) (6).

Several pieces of evidence suggest that cataracts contain insoluble calcium salts (7–13). Our recent studies in two mouse models of cataract have shown that lenses expressing a mutant lens fiber cell connexin, Cx46fs380 or Cx50D47A, have high intracellular concentrations of free Ca^{2+} that are beyond the K_{sp} for several of its salts and contain calcium precipitates. Importantly, the three-dimensional distribution of the calcium salt deposits resembles the morphology and location of the cataracts (14–16). These observations suggested that the formation of calcium precipitates might be part of a common mechanism of cataract development.

To test the generality of the proposed pathogenic mechanism, we studied a mouse model in which cataracts develop due to a mutation in one of the γ-crystallin genes. These mice were available as live animals from a major commercial vendor, so they seemed ideal to pursue our studies. Here, we report the results of our extensive characterization of these mouse lenses. These experiments have yielded data that provide further support for the importance of calcification in cataractogenesis.

Results

We previously showed that the lenses of mice carrying connexin mutations, Cx46fs380 or Cx50D47A, stained with Alizarin red in a pattern morphologically similar to the cataract (14, 15). To test the generality of this finding beyond mice with connexin mutations, we obtained mice from the Jackson Laboratory that allegedly expressed a γB-crystallin mutation that was linked to the development of cataracts in mice, γB^{S11R}-crystallin (17). These mice had a mutation that arose spontaneously in the A/J strain and were backcrossed for several generations into the C57BL/6J strain. We used the genotyping approach previously employed by Li *et al.* (17) and confirmed that the phenotype co-segregated with the

‡ These authors share senior authorship.
* For correspondence: Viviana M. Berthoud, vberthou@bsd.uchicago.edu.

D1Mit156 satellite marker located in chromosome 1. According to this method, the different genotypes could be distinguished based on the difference in amplicon size between the A/J and C57BL/6J strains for the satellite marker D1Mit156 located in chromosome 1 (112 bp vs. 143 bp). We also confirmed that the homozygous mutant lenses had a pronounced central cataract unlike the wild-type lenses that were transparent (Fig. 1). The central cataract appeared surrounded by multiple little opacities located between the cortex and the nucleus; their distribution had a shamrock-like form in the example shown in Figure 1.

During the COVID-19 outbreak, we outsourced the genotyping to Transnetyx who designed primers to differentiate between wild-type and mutant γB^{S11R}-crystallin mice by real-time PCR. However, analysis of all samples yielded a wild-type genotype. To verify the results of this genotyping, we amplified the sequence encoding γB-crystallin by PCR from genomic DNA. Sequencing of this amplicon showed no mutation, suggesting that the spontaneous cataract in these mice corresponded to a different genetic variant that mapped to the same region of chromosome 1. Therefore, we deemed it essential to identify the mutation and to characterize the alterations in these lenses.

Identification of the mutation in the mutant mice

To identify the mutant gene, we performed whole genome sequencing on genomic DNA prepared from homozygous mutant mice. A significant number of nucleotide variations that corresponded to differences between the genomic sequences of the C57BL/6J and the A/J strains were found in a region of chromosome 1. This is consistent with the PCR results indicating that the cataract phenotype co-segregated with the satellite marker D1Mit156. When this region of chromosome 1 was analyzed, no nucleotide mutations or variations were found in the γB-crystallin gene compared to the genomic DNA sequence from the A/J strain (https://www.ncbi.nlm.nih.gov/nuccore/CM003954.1). However, analysis of other genes in this region revealed a 5-bp duplication within the sequence encoding γC-crystallin, BC056454.1:c.409_413dup (Fig. 2*A*). γC-crystallin is a member of the γ-crystallin family whose expression in the mouse lens starts early in development, at 11.5 dpc (18, 19), and it continues to be expressed in both epithelial and fiber cells as demonstrated at the RNA and protein levels (20–23). For simplicity, we will refer to the BC056454.1:c.409_413dup mutation as $Crygc^{dup}$. The predicted protein product corresponding to this mutation is GRYGC p.(Pro138fs).

The secondary structure of the β- and γ-crystallins contains four Greek key motifs, each consisting of about 40 amino acids that fold into four consecutive anti-parallel strands (Fig. 2*B*). Two consecutive Greek key motifs (*i.e.*, first and second and third and fourth) intercalate in a symmetrical manner to form two wedge-shaped domains filled with hydrophobic side chains that are connected by an interdomain linker (24). The 5-bp nucleotide duplication in $Crygc^{dup}$ is located right before the DNA sequence that encodes the first amino acid of the loop connecting Greek key motifs 3 and 4 within the CRYGC protein. This causes a frameshift that results in the translation of an aberrant sequence, early termination of the protein, and loss of Greek key motif 4 (Fig. 2*C*).

We found no other substitutions in the coding sequences of other crystallin genes in this region when compared to genomic DNA from the A/J strain.

Heterozygous mice develop cataracts at much older ages than homozygotes

Darkfield microscopy examination showed no difference in the appearance or transparency of lenses from young heterozygous mutant or wild-type mice (not shown). However, the lenses of heterozygous mice developed small nuclear opacities encircled by a halo as the mice grew older (Fig. 3). The initial detectability of these changes varied between individuals, ranging from 60 to 90 days of age. By 120 days of age and at later ages, these opacities were more

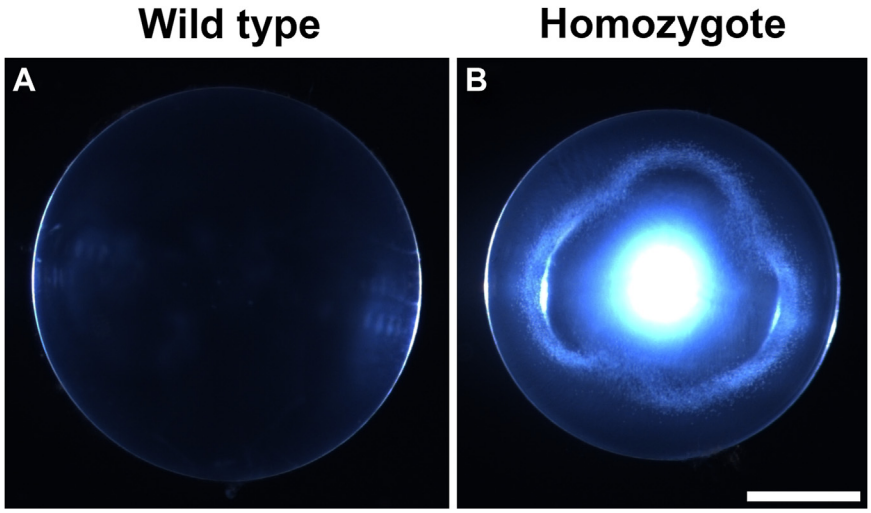

Figure 1. Homozygous crystallin mutant mice develop severe cataracts. *A* and *B*, *darkfield* images of the lenses from a 26-day-old wild-type C57BL/6J mouse (*A*) and a 23-day-old homozygous crystallin mutant mouse (*B*). Scale bar = 600 μm.

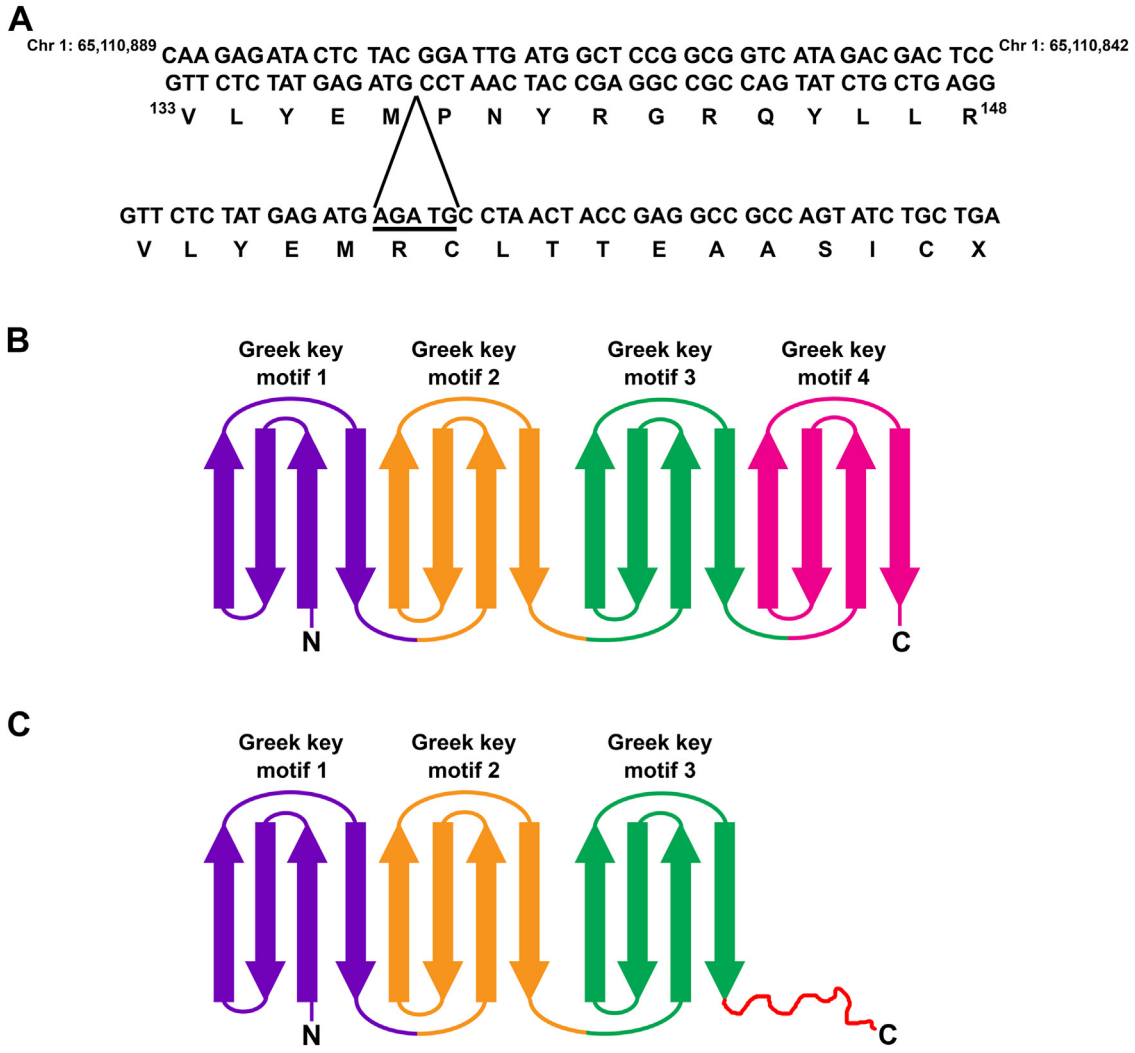

Figure 2. The mutant mice have a 5-bp duplication in the γC-crystallin (*Crygc*) gene. *A*, *top*, DNA sequence of a region of mouse chromosome 1 from the GRCM39 mouse genome assembly encoding part of γC-crystallin. The encoded wild-type amino acid sequence is shown underneath. *Bottom*, DNA sequence of the same region of chromosome 1 from a homozygous *Crygc* mutant mouse showing the site of insertion of the 5-bp duplication (*underlined* nucleotide sequence). The resulting amino acid sequence is shown underneath. The 5-bp duplication results in a frameshift and an early termination of the protein. *B*, diagram of the wild-type protein with its four *Greek key motifs*. *C*, diagram of the mutant protein. The frameshift occurs after the third *Greek key motif* (*red squiggly line*) and the resulting mutant protein lacks the fourth *Greek key motif*. C, C-terminus; N, N-terminus.

abundant and pronounced than ones occasionally observed in wild-type lenses (Fig. 3). Regardless, heterozygotes never developed as severe opacities as observed in the homozygotes.

Crystallin levels are decreased by expression of Crygc^{dup}

Previous biochemical studies of crystallins predict that the presence of an aberrant sequence after the third Greek key motif and the absence of the fourth motif in the mutant protein would perturb the normal secondary and tertiary structures, altering protein stability and/or solubility (for a review see (25)). To test whether levels of crystallins were altered by the expression of the γC-crystallin mutant, we determined the abundance of crystallins in total lens homogenates. Levels of αA- and βB1-crystallins were decreased in the total homogenates from heterozygous and homozygous mutant lenses (to 65% and 53% of the wild-type values for αA-crystallin and to 67% and 58% of the wild-type values for βB1-crystallin, respectively). No significant changes were detected in levels of αB-crystallins. Levels of γ-crystallins were decreased in the total homogenates from homozygous mutant lenses (to 68% of the wild-type values), but they were not significantly changed in total homogenates of lenses from heterozygotes (Fig. 4).

To assess possible changes in the solubility of the crystallins, we prepared aqueous-soluble and aqueous-insoluble fractions and analyzed these fractions by immunoblotting. The soluble fractions contained essentially all of the crystallin in these samples. No bands were detected in the blots of insoluble fractions that were exposed together with corresponding amounts of the total and soluble fractions. However, after extremely long overexposure of the films, a very faint band of γ-crystallins was observed in some (but not all) of the aqueous-insoluble fractions from heterozygous and homozygous mutant lenses (Fig. 4*F*).

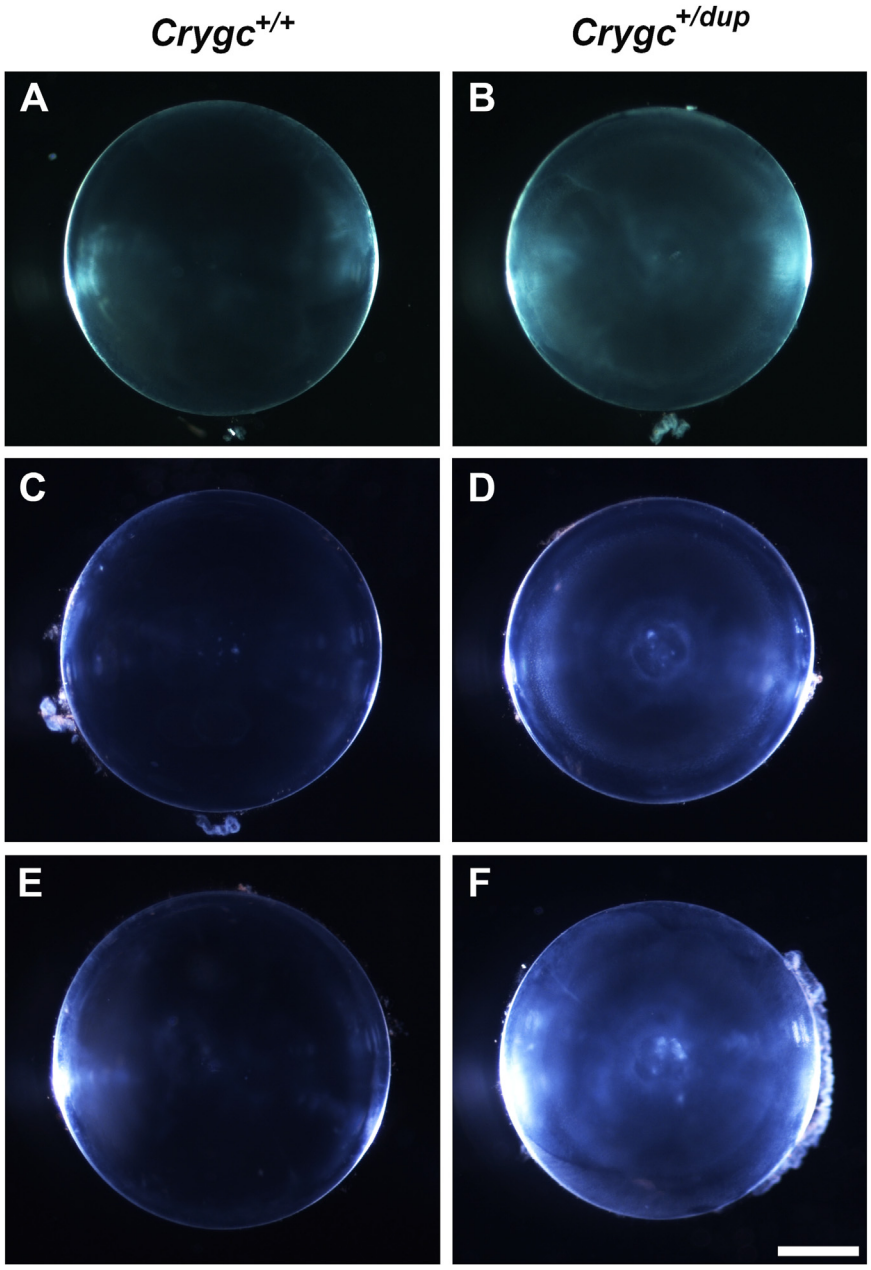

Figure 3. Heterozygous crystallin mutant mice develop mild cataracts with age. The lenses from wild-type (*Crygc*$^{+/+}$; *A*, *C*, and *E*) and heterozygous crystallin mutant (*Crygc*$^{+/dup}$; *B*, *D*, and *F*) mice at 90 (*A* and *B*), 120 (*C* and *D*), and 213 (*E* and *F*) days of age were photographed using darkfield illumination. A very faint opalescence is detected in the example shown for the 90-day-old heterozygous lens (*B*). By 120 days of age (*D*), heterozygous mutant lenses show several minor opacities in the nuclear region and a halo that encircles them. The number, intensity, and size of nuclear opacities are more pronounced at 213 days of age (*F*). Scale bar = 600 μm.

We also used the pattern of bands in the immunoblots to evaluate possible alterations in the integrity of crystallins. αA- and -αB-crystallins were detected as single bands, and γ-crystallins were detected as a doublet in both wild-type and mutant lenses. However, a faint band of βB1-crystallins with a faster electrophoretic mobility than the main band was detected in the total homogenates and aqueous-soluble fractions from homozygous mutant lenses, suggesting a minor amount of cleavage for this crystallin (Fig. 4*C*). Upon overexposure of the films, a βB1-crystallin band migrating at the same mobility was also observed in the total homogenates and aqueous-soluble fraction from heterozygous mutant lens samples (Fig. 4*E*). Similarly, after extremely long overexposure of the films, a very faint band of γ-crystallins migrating faster than the doublet was detected in the total homogenates and aqueous-soluble fractions from heterozygous and homozygous mutant lenses (Fig. 4*F*). Thus, in contrast to the results reported for the γB^{S11R}-crystallin heterozygous and homozygous mice (17), we detected minimal amounts of cleaved βB1- and γ-crystallins (barely above the detection limit of the method) and no cleaved forms of αA- and αB-crystallins in the *Crygc*^{dup} lenses.

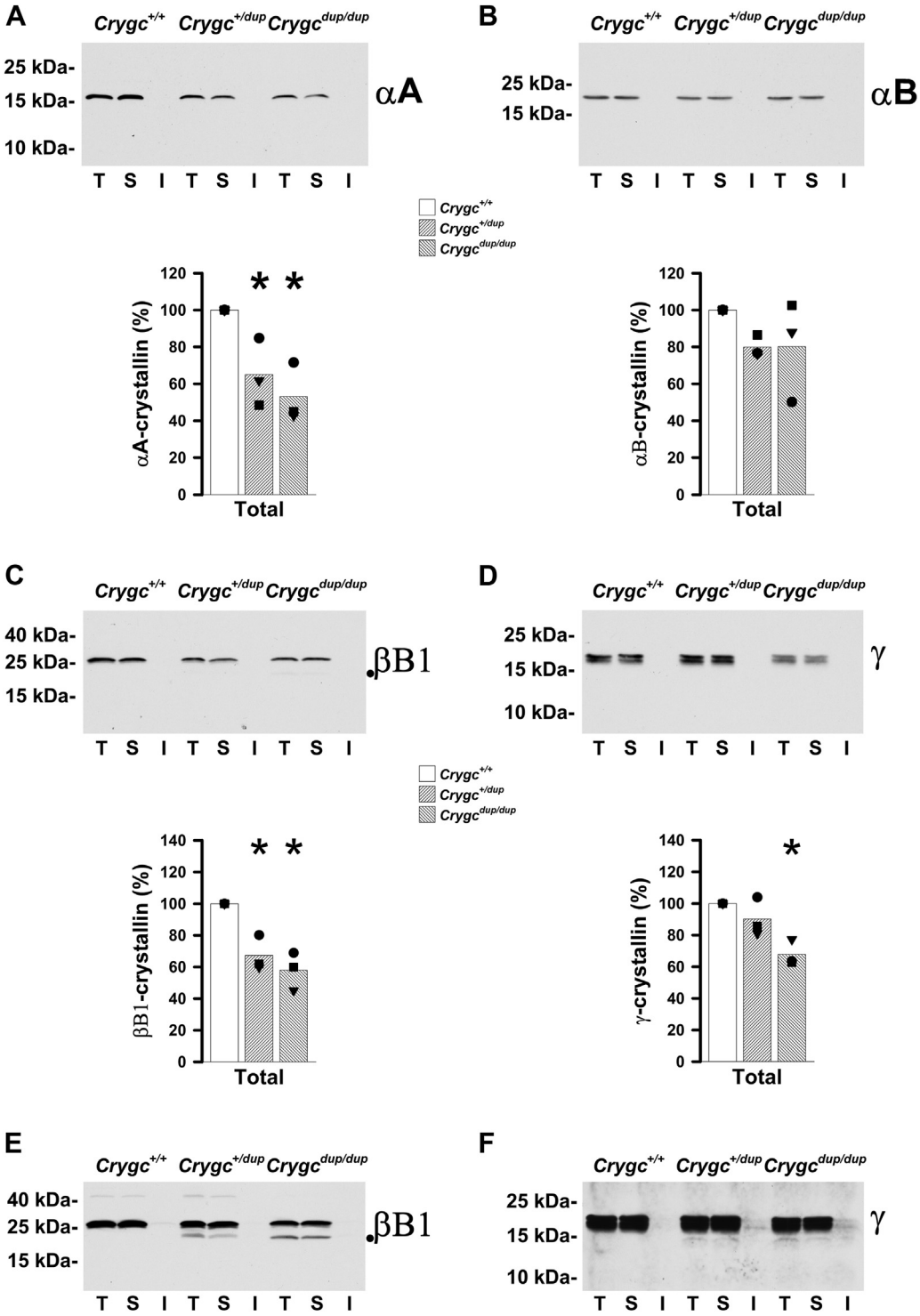

Figure 4. Expression of the γC-crystallin mutant decreases total levels of crystallins but does not lead to major effects on their solubility. *A–D*, immunoblots illustrate levels of αA- (*A*), αB- (*B*), βB1- (*C*), and γ- (*D*) crystallins in whole lens homogenates (T), and lens aqueous-soluble (S) and aqueous-insoluble (I) fractions from 30- to 32-day-old wild-type (*Crygc*$^{+/+}$), heterozygous mutant (*Crygc*$^{+/dup}$), and homozygous mutant (*Crygc*$^{dup/dup}$) mice. Total levels of αA- and βB1-crystallins were decreased in heterozygous mutant lenses, while total levels of αA-, βB1- and γ-crystallins were decreased in homozygous mutant lenses. A faint βB1-crystallin band of faster electrophoretic mobility was detected in the total homogenate and aqueous-soluble fraction of homozygous mutant lenses (its position is marked with a *dot* in panel *C*). Graphs show the average of the densitometric values of the bands obtained in the total homogenates after quantification of the bands detected in three independent experiments (*black symbols*, one for each set containing all three genotypes). For each experiment, values were normalized to the value determined in the total homogenate of the wild-type lens for the corresponding crystallin (which was set to 100%). *Asterisks* indicate values that differed significantly from the levels in the total homogenate of the wild-type mice. *E*, example illustrating the appearance of the faster electrophoretic mobility βB1-crystallin band in the total homogenates and aqueous-soluble fractions of heterozygous mutant (*Crygc*$^{+/dup}$) and homozygous mutant (*Crygc*$^{dup/dup}$) lenses after long overexposure of the X-ray film. *F*, example illustrating the slight bands of γ-crystallin detected in the insoluble fraction of some heterozygous mutant (*Crygc*$^{+/dup}$) and homozygous mutant (*Crygc*$^{dup/dup}$) lenses after extremely long overexposure of the X-ray film. The example also illustrates the appearance of a very faint band that migrates faster than the doublet in the total homogenates and aqueous-soluble fractions from heterozygous (*Crygc*$^{+/dup}$) and homozygous (*Crygc*$^{dup/dup}$) mutant lenses.

Crygc^{dup} lenses show impaired fiber cell organization and differentiation

Because crystallins have been implicated as participating in lens development, fiber cell morphology, and maturation (26), we investigated whether the expression of *Crygc^{dup}* affected lens fiber cell organization and differentiation. Staining with wheat germ agglutinin (WGA), which binds to plasma membrane glycoproteins, revealed a striking disorganization of the fiber cells in the nuclear region of homozygous lenses (Fig. 5). At 10 days of age, the central fiber cells were highly variable in dimension and orientation. The central region of heterozygous lenses showed only minor disturbances compared to the wild-type lenses (Fig. 5). Denucleation was also affected in heterozygous and homozygous *Crygc^{dup}* lenses. Nuclei and nuclear remnants were detected in more central regions of mutant lens sections, especially in those from homozygous lenses (Fig. 5). In

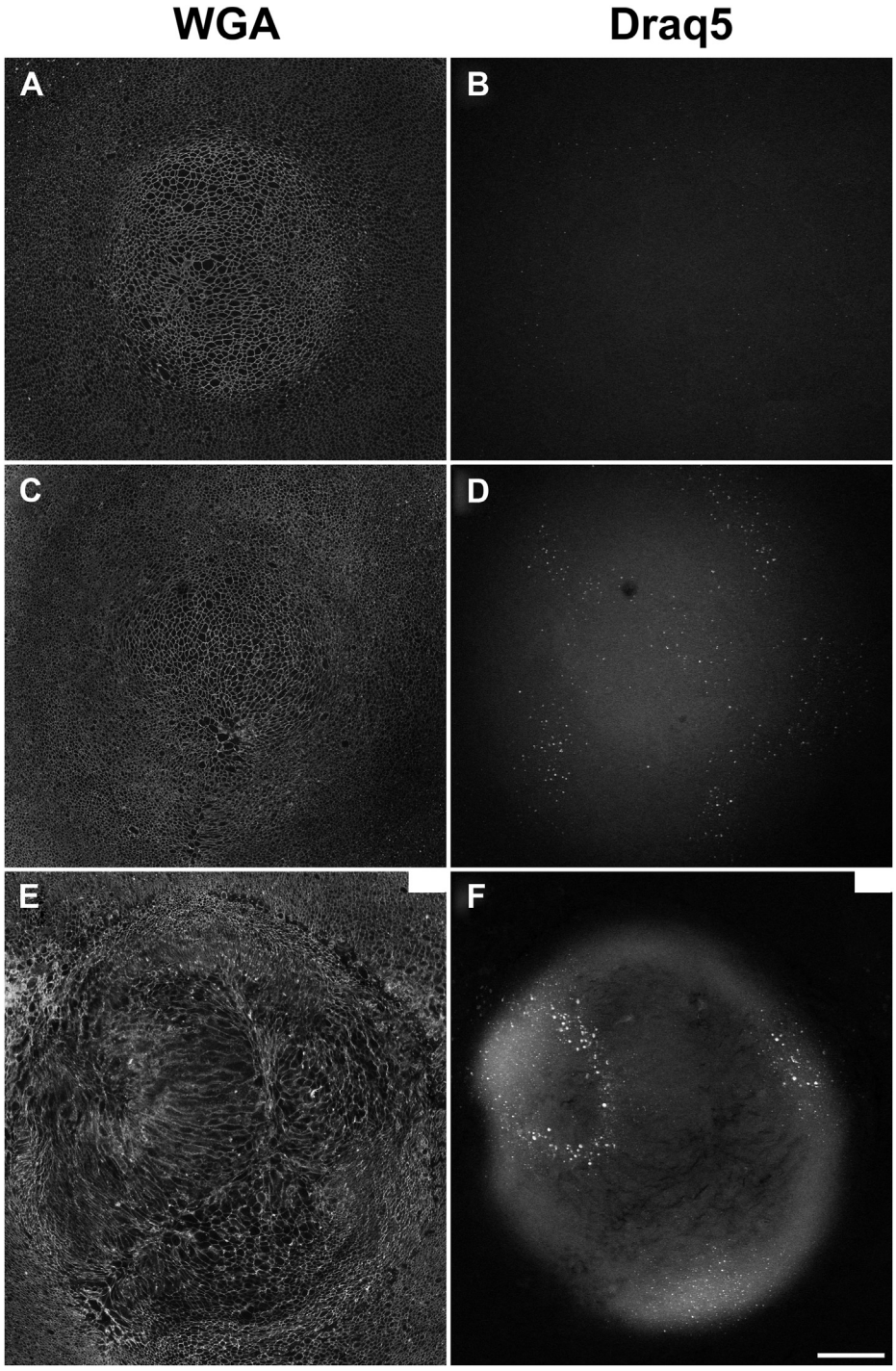

Figure 5. Cellular organization and denucleation are impaired in *CrygC^{dup}*-expressing lenses. *A–F*, confocal images show the distributions of wheat germ agglutinin (WGA; *A*, *C* and *E*) and Draq5-stained nuclei and nuclear remnants (*B*, *D*, and *F*) in equatorial sections from 10-day-old lenses of wild-type (*Crygc$^{+/+}$*; *A* and *B*), heterozygous mutant (*Crygc$^{+/dup}$*; *C* and *D*), and homozygous mutant (*Crygc$^{dup/dup}$*; *E* and *F*) mice. Scale bar: 100 μm.

agreement with this observation, levels of histone H3 in homozygous lenses were increased to 472% of wild-type values. In heterozygous lenses, levels of histone H3 were on average 240% of the wild-type values; however, comparison of their values did not reach statistical significance ($p = 0.08$), likely due to the large variability between individuals (Fig. 6*C*). Levels of the ER-resident 78 kDa glucose-regulated protein (GRP78) were increased to 119% and 264% in heterozygous and homozygous *Crygc*^{dup} lenses compared to the levels in lenses from wild-type littermates (Fig. 6*A*). Similarly, levels of the translocase of outer mitochondrial membrane 20 (TOM20) were increased in heterozygous and homozygous mutant lenses (Fig. 6*B*); they represented 124% and 267% of the values in wild-type lenses.

Expression of Crygc^{dup} *alters levels and distribution of fiber cell connexins*

Because mutations in other lens membrane and soluble proteins (27), including crystallins (28, 29), can affect levels of lens fiber cell connexins, we determined the levels of Cx46 and Cx50 in the γC-crystallin mutant lenses by immunoblotting of lens homogenates. At 30 days of age, levels of Cx46 were significantly decreased to 20% (heterozygotes) and 11% (homozygotes), and levels of Cx50 were significantly decreased to 27% (heterozygotes) and 26% (homozygotes), compared to the levels in lenses from wild-type littermates (Fig. 7, *A* and *B*).

Connexin mRNA levels were analyzed to determine if the changes in connexin protein levels could reflect changes in the transcription of *Gja3* (Cx46) and/or *Gja8* (Cx50). At 30 days of age, the connexin mRNA levels in heterozygous and homozygous mutant lenses were similar to those of wild-type lenses (Fig. 7, *C* and *D*). Thus, changes in transcription are unlikely to explain the decrease in connexin levels.

To determine whether the expression of *Crygc*^{dup} also affected the distribution of connexins, we performed immunofluorescence in combination with staining of filamentous actin (to delineate individual fiber cells). The distribution and abundance of immunoreactive Cx46 were similar in the most superficial lens fiber cells in wild-type lenses and in heterozygous and homozygous mutant lenses. However, in more interior fiber cell layers, the distribution of Cx46 appeared patchy and irregular in both heterozygous and homozygous mutant lenses. Very little (if any) immunoreactive Cx46 was detected in more central fiber cell layers (unlike the abundant Cx46 immunoreactive gap junction plaques present in wild-type lenses that extended deep into the lens) (Fig. 8). The distribution and abundance of Cx50 in gap junction plaques were also markedly affected by the expression of the γC-crystallin mutant. Both heterozygous and homozygous mutant lenses showed a patchy distribution with a scarcity of Cx50 immunoreactive plaques even in the most superficial lens fiber cells compared to wild-type lenses (Fig. 9). These changes became even more pronounced in more interior fiber cells (Fig. 9). In addition, heterozygous and homozygous mutant lenses continued to show irregularities in the pattern of phalloidin staining,

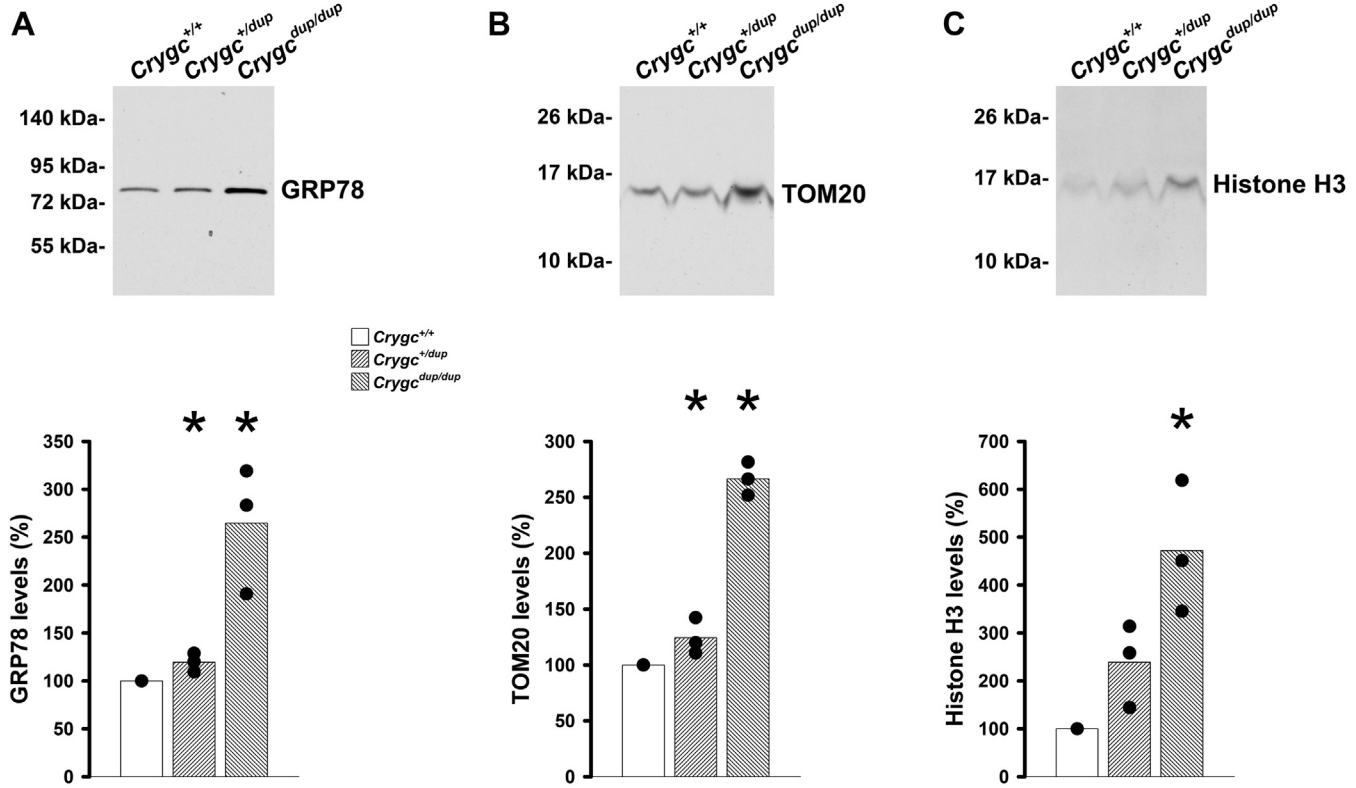

Figure 6. Expression of *CrygC*^{dup} impairs lens cell differentiation. *A–C*, immunoblots of GRP78 (*A*), TOM20 (*B*), and histone H3 (*C*) in whole lens homogenates from wild-type (*Crygc*$^{+/+}$), heterozygous mutant (*Crygc*$^{+/dup}$), and homozygous mutant (*Crygc*$^{dup/dup}$) mice at 30 days of age. The migration positions of the molecular mass markers are indicated on the left. Graphs show the quantification of the immunoreactive bands obtained in independent experiments (*black circles*). The bars represent the averages of the values obtained for each genotype (n = 3). Significant differences between wild-type and heterozygous mutant lenses or wild-type and homozygous mutant lenses are indicated by *asterisks* ($p < 0.05$).

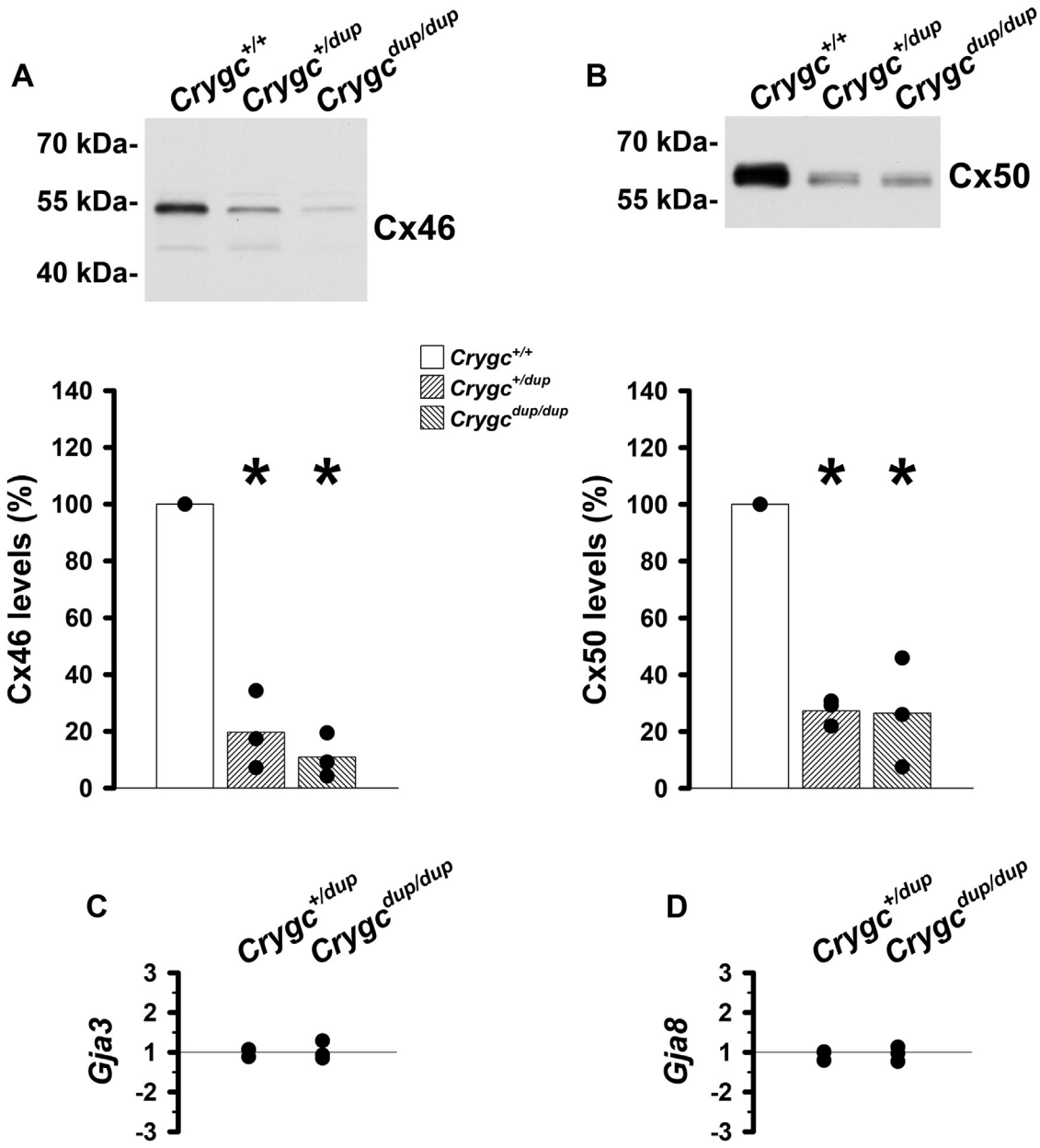

Figure 7. Expression of the crystallin mutant alters levels of Cx46 and Cx50 proteins but not their transcripts at 1 month of age. *A* and *B*, immunoblots of Cx46 (*A*) and Cx50 (*B*) in whole lens homogenates from wild-type (*Crygc*$^{+/+}$), heterozygous mutant (*Crygc*$^{+/dup}$), and homozygous mutant (*Crygc*$^{dup/dup}$) mice at 30 days of age. The migration positions of the molecular mass markers are indicated on the *left*. Graphs show the quantification of the immunoreactive bands obtained in independent experiments (*black circles*). The bars represent the averages of the values obtained for each genotype (n = 3). Significant differences between wild-type and heterozygous mutant lenses or wild-type and homozygous mutant lenses are indicated by *asterisks* ($p<0.05$). *C* and *D*, graphs show the fold change of the transcript levels for *Gja3* (Cx46 transcript; *C*) and *Gja8* (Cx50 transcript; *D*) in 30-day-old heterozygous (*Crygc*$^{+/dup}$) and homozygous (*Crygc*$^{dup/dup}$) mutant lenses relative to wild-type littermate lenses (*Crygc*$^{+/+}$) as determined by Reverse Transcription Real-Time PCR. The values obtained in each of three independent experiments are shown in *black circles*. The value obtained in wild-type lenses was considered as 1.

especially toward the center of the lens, compared to the regular pattern of phalloidin staining showing radial columns of fiber cells in cross-sections of wild-type lenses.

Gap junction-dependent intercellular communication is decreased in Crygc^{dup}-expressing lenses

The significant decrease in levels and the lack of immunoreactive Cx46 and Cx50 gap junction plaques in interior fiber cells led us to assess gap junctional coupling between fiber cells in these lenses. Therefore, we determined the series resistance, which corresponds to the reciprocal of gap junctional coupling. The series resistance is the resistance between the point of recording and the lens surface due to the parallel resistivities of intracellular and extracellular pathways $(R_iR_e)/(R_i + R_e)$. In the usual situation, $R_e \gg R_i$, so $(R_iR_e)/(R_i + R_e) \cong R_i$. The series resistance increased from wild-type to heterozygous to homozygous lenses with the most significant increase in homozygous lenses (Fig. 10). The values of gap junctional coupling conductance for wild-type, heterozygous, and

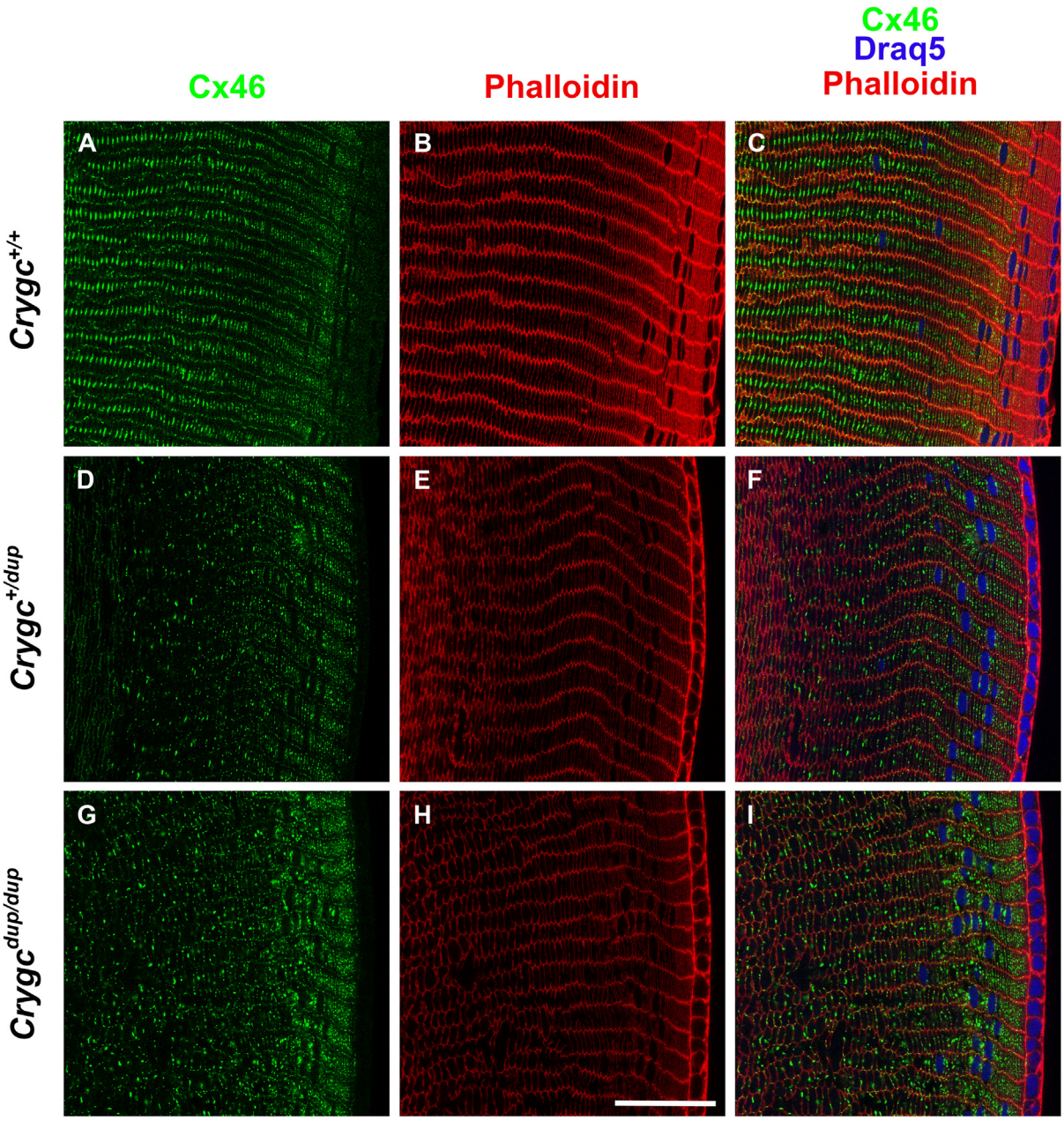

Figure 8. The immunoreactive pattern of distribution of Cx46 is altered in lenses expressing the crystallin mutant. *A–I*, confocal images show the distributions of immunoreactive Cx46 (*green*; *A*, *D* and *G*) and filamentous actin (phalloidin, red; *B*, *E* and *H*) in cross sections from lenses of wild-type (*Crygc*$^{+/+}$; *A–C*), heterozygous mutant (*Crygc*$^{+/dup}$; *D–F*), and homozygous mutant (*Crygc*$^{dup/dup}$; *G–I*) mice at 46 to 48 days of age. The merged images for the two fluorescence signals and the nuclei stained with Draq5 are shown on the right (*C*, *F* and *I*). Scale bar: 45 μm.

homozygous mutant lenses are presented in Table 1. Gap junctional coupling conductance in differentiating fibers (G_{DF}) from heterozygous and homozygous mutant lenses decreased to 52% and 36% of the value in wild-type lenses, respectively. The intracellular resistivity in the mature fiber cell domain (MF) in the homozygous (*Crygc*$^{dup/dup}$) lenses was about 98 KΩcm; this is essentially the value of the effective extracellular resistivity (R_e), implying that R_i approaches infinity, or $G_{MF} \cong 0$. In the heterozygous (*Crygc*$^{+/dup}$) lenses, G_{MF} was reduced to 55% of the wild-type value (Table 1).

One surprising observation in these lenses was that R_e was 100 KΩcm (Table 2), much higher than the values of 20–30 KΩcm determined in previous mouse lens studies (30). The surface membrane conductance (G_S) was essentially constant at about 0.4 mS/cm^2 independent of genotype. The fiber cell membrane conductance (g_m) dropped from about 3 S/cm^2 in wild-type lenses to about 2 S/cm^2 in heterozygous and homozygous mutant lenses. This change is not that large, and it is not progressive as one would expect if it were a direct result of the mutation of γC-crystallin. Either value is in the range typically measured in other studies; thus, most likely the

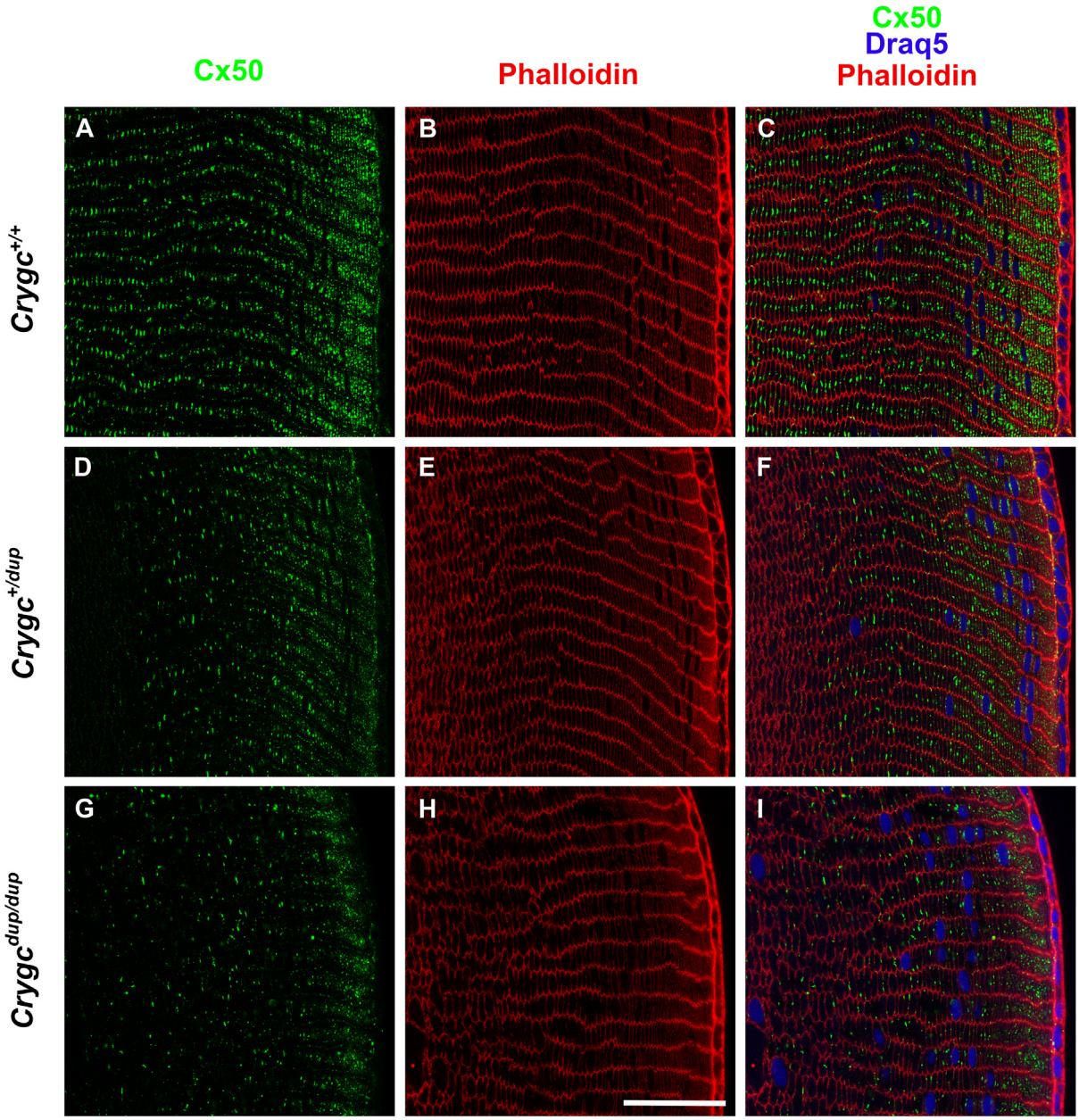

Figure 9. The distribution of immunoreactive Cx50 is decreased in lenses expressing the crystallin mutant. *A–I*, confocal images show the distributions of immunoreactive Cx50 (*green*; *A*, *D* and *G*) and filamentous actin (phalloidin, red; *B*, *E*, and *H*) in cross sections from lenses of wild-type (*Crygc*$^{+/+}$; *A–C*), heterozygous mutant (*Crygc*$^{+/dup}$; *D–F*), and homozygous mutant (*Crygc*$^{dup/dup}$; *G–I*) mice at 46 to 48 days of age. The merged images for the two fluorescence signals and Draq5-stained nuclei are shown on the right (*C*, *F*, and *I*). Scale bar: 45 μm.

apparent decrease reflects biological variation and experimental uncertainty in the complex process of recording and curve-fitting the data.

Table 1
Gap junctional conductance is decreased in *Crygc*^{dup}-expressing lenses

Genotype	G_{DF} (S/cm^2)	G_{MF} (S/cm^2)	n
Crygc$^{+/+}$	0.98	0.67	8
Crygc$^{+/dup}$	0.51	0.37	12
Crygc$^{dup/dup}$	0.35	0.0	12

The Table shows the gap junctional coupling conductance per area of radial cell-to-cell contact for differentiating fibers (G_{DF}) and mature fibers (G_{MF}), calculated as the inverse of the best fit of the effective intracellular resistivity ($R_{DF,MF}$) to series resistance data multiplied by the width (w) of a fiber cell ($G_{DF,MF} = 1/(R_{DF,MF} \cdot w)$), where w = 3 μm. n represents the number of lenses studied to compile the series resistance data shown in Figure 10.

Crygc$^{dup/dup}$ *lenses contain material that stains with Alizarin red*

The decrease in gap junction-mediated intercellular coupling between fiber cells of the γC-crystallin mutant lenses suggested that the circulation of ions within the lens was

Table 2
Impedance-derived parameters in *Crygc* mouse lenses

Genotype	G_S (mS/cm^2)	g_m (μS/cm^2)	R_e (KΩcm)	n
Crygc$^{+/+}$	0.35 ± 0.23	2.78 ± 1.23	104 ± 31	8
Crygc$^{+/dup}$	0.43 ± 0.15	1.61 ± 1.19	104 ± 42	7
Crygc$^{dup/dup}$	0.37 ± 0.19	1.69 ± 0.86	81 ± 16	9

The Table presents the values of conductance per area of membrane for surface cells (G_S) and fiber cells (g_m), and the effective extracellular resistivity (R_e) based on curve fits. n is the number of lenses studied.

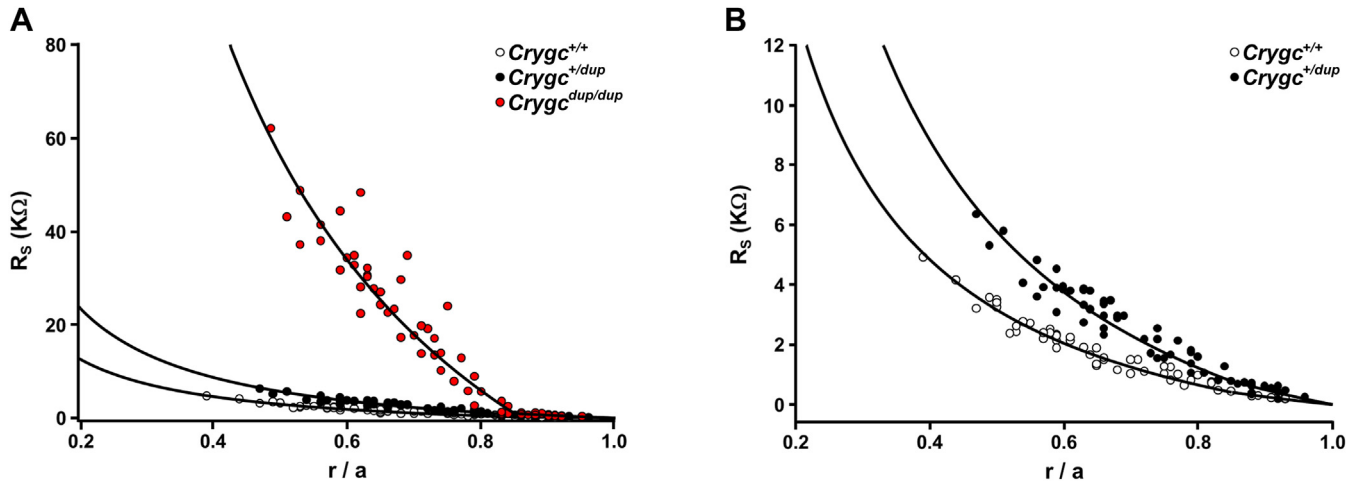

Figure 10. Lenses from mice expressing the crystallin mutant have decreased gap junctional conductance. *A*, graph shows the series resistance (Rs) due to gap junctions coupling fiber cells between the point of recording and the surface of the lens from 91- to 118-day-old wild-type (*Crygc*$^{+/+}$), heterozygous mutant (*Crygc*$^{+/dup}$) and homozygous mutant (*Crygc*$^{dup/dup}$) lenses. Data are graphed as a function of radial distance from the lens center (r; cm), normalized to the lens radius (a; cm). *B*, graphical comparison of the data from wild-type (*Crygc*$^{+/+}$) and heterozygous mutant (*Crygc*$^{+/dup}$) lenses to illustrate more clearly the increase in series resistance in heterozygous mutant lenses.

impaired (30). This would be predicted to result in the accumulation of ions such as calcium, which could precipitate if their concentration surpasses the K_{ps} of its salts. To test this, we prepared insoluble fractions from wild-type, heterozygous and homozygous lenses and stained them with Alizarin red, a dye that stains calcium deposits within tissues. Most preparations of wild-type and heterozygous lens insoluble fractions did not contain any Alizarin red-stained particles (Fig. 11, *A*, *B* and *D*). Very rarely, lightly stained small particles were found in wild-type and heterozygous lens preparations (not shown), consistent with the small nuclear cataracts detected in wild-type and heterozygous *Crygc*$^{+/dup}$ lenses (Fig. 3). In contrast, particles strongly stained with Alizarin red were abundant and detected in all of the insoluble fraction preparations from homozygous lenses (Fig. 11, *C* and *E–L*).

To study the three-dimensional distribution of the Alizarin red particles in the homozygous mutant lenses, we acquired darkfield images from the lenses followed by whole-mount staining with Alizarin red. Wild-type lenses from littermates were used as controls. While wild-type lenses showed no remarkable staining, homozygous *Crygc*$^{dup/dup}$ mutant lenses showed pronounced staining with Alizarin red in the central region with an overall distribution in the same region occupied by the cataract (Fig. 12, *A–D*).

Micro-computed tomography scanning reveals mineralized material in Crygc$^{dup/dup}$ lenses

The presence of Alizarin red-stained particles in these lenses led us to examine them for the presence of mineralized material and to determine its three-dimensional distribution using high energy, micro-computed tomography (micro-CT) scanning. Freshly dissected wild-type and homozygous lenses were photographed by darkfield microscopy; then, they were fixed and studied by micro-CT scanning. No radio-dense material was detected in the micro-CT images from wild-type lenses, but the *Crygc*$^{dup/dup}$ lenses contained abundant radio-dense material in mice of both sexes (Fig. 13).

Crygc$^{dup/dup}$ lenses showed widely dispersed particles with a moderate X-ray density (but above the background for the lens) with most of the X-ray dense regions in curved, acicular shapes. The total X-ray dense material (a combination of scattered particles of moderate X-ray density and of higher X-ray density) occupied a spherical volume that encompassed the region of the cataract in each lens (Fig. 13 and Movie S1).

Infrared microspectroscopy identifies the lens mineral in Crygc$^{dup/dup}$ lenses as apatite, a form of calcium phosphate

To determine the composition of the mineral particles, sections from homozygous *Crygc*$^{dup/dup}$ lenses were analyzed using attenuated total internal reflection Fourier-transform infrared microspectroscopy (ATR-μFTIR) imaging. Localization of Ca^{2+}-containing material in Yasue-stained sections facilitated the identification of regions in adjacent sections to analyze by ATR-μFTIR (Fig. 14). Representative spectra extracted from the non-mineral regions showed the characteristic spectral bands for normal proteins, which include the combined N-H and O-H stretch located near 3,274 cm^{-1} and the amide I and II absorptions located near 1,634 and 1,522 cm^{-1}, respectively (Fig. 14, non-mineral region). Representative spectra extracted from the mineral-rich regions showed several absorption bands in addition to those corresponding to protein (Fig. 14, mineral region). The additional absorptions in the mineral-rich regions were located at 1,098, 1,026, 960, and 877 cm^{-1}, which are characteristic of calcium apatite (Fig. 14). A reference spectrum of apatite is shown in Figure 14 for comparison.

Discussion

In this article, we identified a novel γC-crystallin mutation (*CrygC*^{dup}) that causes cataracts, and we have provided some

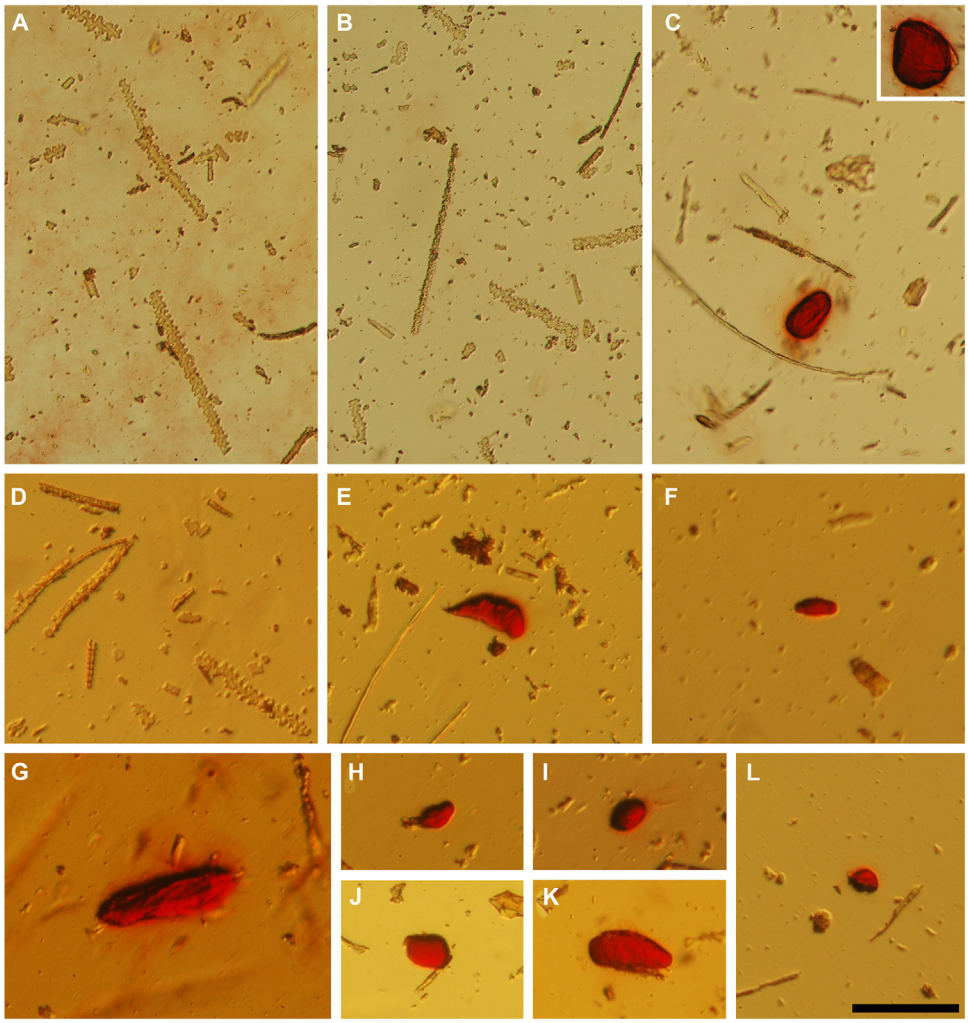

Figure 11. Particles in the insoluble fractions of *Crygc*$^{dup/dup}$ lenses stain with Alizarin red. *A–C*, photographs of material present in lens insoluble fractions from 60-day-old wild-type (*A*), heterozygous (*B*), and homozygous (*C*) mice after resuspension and reaction with Alizarin red. *D–F*, photographs of material present in lens insoluble fractions from 111-day-old wild-type (*D*) and homozygous crystallin mutant (*E* and *F*) mice after resuspension and reaction with Alizarin red. *C*(*inset*) and *G–L*, photographs show additional examples of Alizarin red-stained particles present in the insoluble fraction of homozygous crystallin mutant lenses. Scale bar: 97 μm for panels *A–C*, 84 μm for panels *D–L*.

insights regarding how this mutation leads to cataractogenesis. Mutations in the γC-crystallin gene (including duplications) have previously been linked to cataracts in humans and in rodents (cat-map.wustl.edu). Several of the previously identified mutations affect Greek key motif 4 in γC-crystallin (cat-map.wustl.edu). The *CrygC*^{dup} mutation identified in our study encodes a protein that contains an aberrant sequence in its C-terminus and lacks the fourth Greek key motif. Although this represents a severe alteration in the secondary and tertiary structure of CRYGC, cataracts in heterozygous *CrygC*^{dup} animals developed much later than in heterozygotes from the previously described *CrygC* mutant mice (31–33). Expression of *CrygC*^{dup} induced several effects that were much more pronounced or only observed in homozygous lenses, including a decrease in levels of γ-crystallins, alteration of nuclear fiber cell morphology and organization, impaired organelle degradation, decreased fiber cell-to-fiber cell gap junctional conductance and formation of calcium precipitates in the form of apatite.

γ-crystallin mutations, lens crystallins, and differentiation

Expression of *Crygc*^{dup} was associated with a decrease in protein levels of αA-crystallins and βB1-crystallin in heterozygous and homozygous lenses, and the appearance of very small amounts of a faster-migrating band of βB1-crystallin. This βB1-crystallin band might represent a calpain-cleaved form (that remained soluble) (34). The reductions in αA-crystallins and βB1-crystallin could be due to the degradation of these crystallins as a result of their interaction with the mutant γC-crystallin. Since αA-crystallins can act as chaperones (1), they may have interacted with the mutant γC-crystallin (to prevent its misfolding) and been degraded together. βB1-crystallin forms complexes with γD-crystallin and suppresses demixing of γD-crystallin (35, 36). Because of the extensive amino acid identity between the members of the γ-crystallin family, it is possible that some βB1-crystallin interacted with the mutant γC-crystallin and was degraded. Alternatively, degradation of βB1-crystallin may have occurred sequentially: initial cleavage by Ca^{2+}-dependent calpains (due to the expected increase in the Ca^{2+} concentration as a result of the decrease in gap junctional

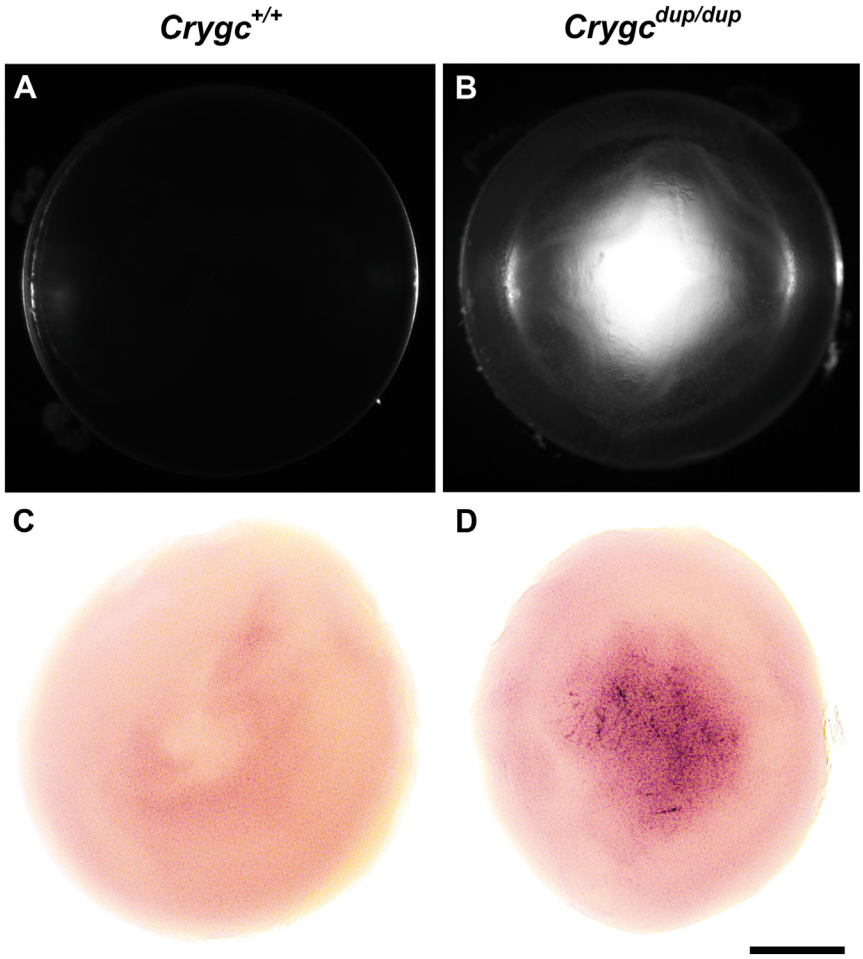

Figure 12. *Crygc*$^{dup/dup}$ lenses stain with Alizarin red. *A* and *B*, photographs of 35-day-old wild-type (*Crygc*$^{+/+}$; *A*) and homozygous crystallin mutant (*Crygc*$^{dup/dup}$; *B*) lenses using darkfield illumination. *C* and *D*, images show the same lenses from the wild-type (*C*) and the homozygote (*D*) after whole-mount staining with Alizarin red. Scale bar: 500 μm for panels *A* and *B*, 385 μm for panels *C* and *D*.

coupling) followed by complete degradation by other proteases. In this case, the faster-migrating band of βB1-crystallin detected in the *CrygC*^{dup} lenses would represent an intermediate step in the degradation process. However, it is unlikely that the reductions of αA- and βB1-crystallins explain the cataract formation because the differences in reductions of these crystallins between heterozygotes and homozygotes were modest compared to the striking differences in phenotype.

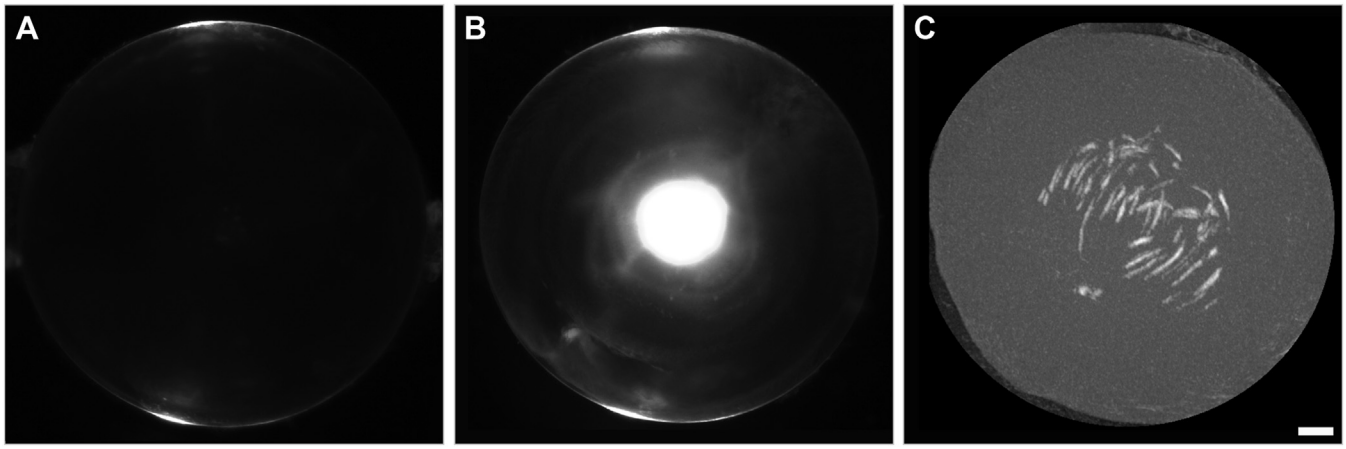

Figure 13. The X-ray dense material in *Crygc*$^{dup/dup}$ lenses occupies the same region as the cataract. *A* and *B*, *darkfield* images of lenses from 60-day-old wild-type (*A*) and homozygous *Crygc*$^{dup/dup}$ (*B*) mice. *C*, Three-dimensional projection of the micro-CT images from the homozygous lens shown in *B*. The scale bar represents 216 μm for panels *A* and *B*, and 200 μm for panel *C*.

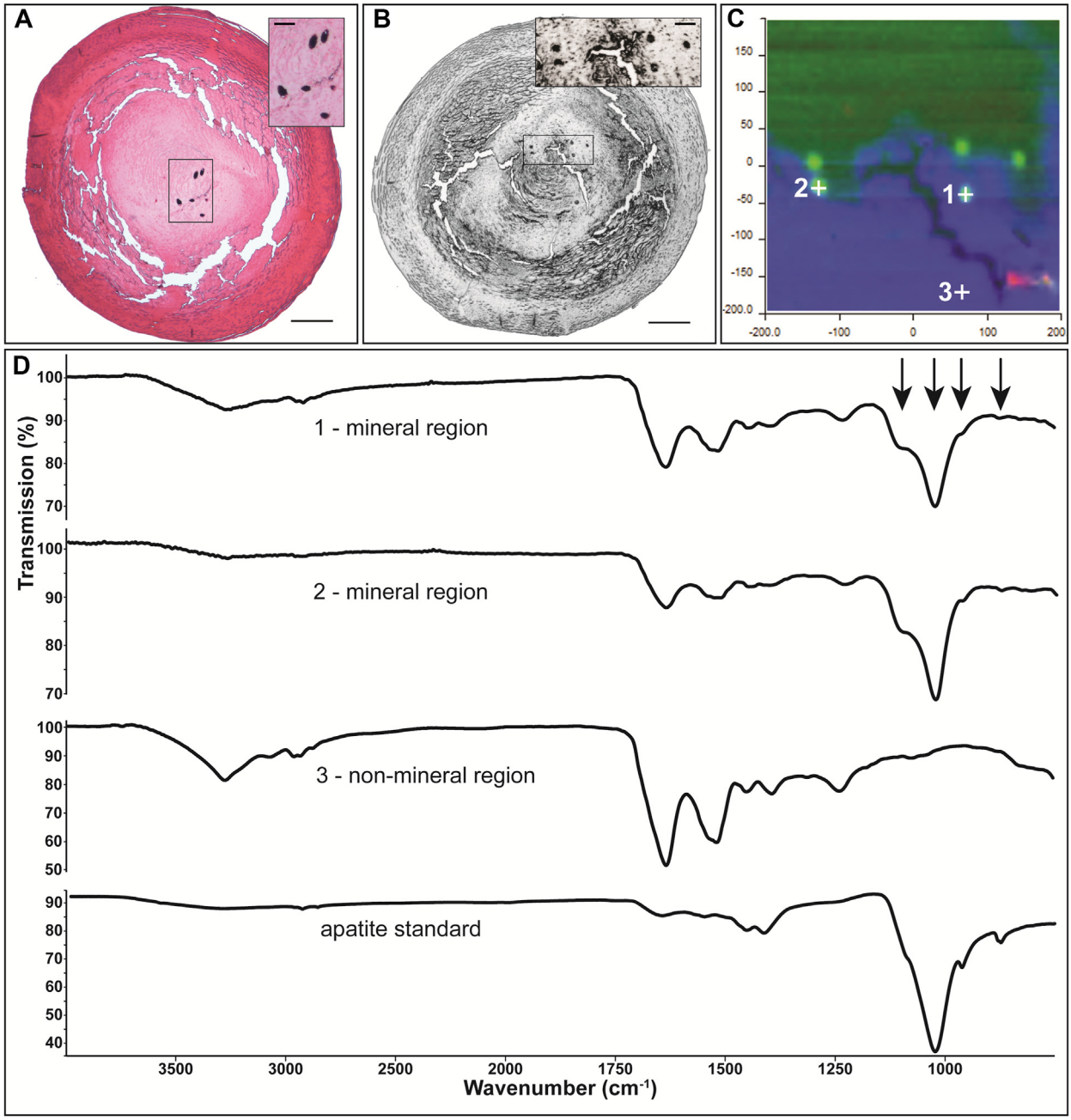

Figure 14. The mineral in *Crygc*$^{dup/dup}$ lenses is apatite. *A*, image showing Yasue staining of a section from the lens of the 60-day-old homozygous *Crygc*$^{dup/dup}$ mouse shown on Figure 13, *B* and *C*. The stained material that appears black corresponds to calcifications. *B*, image of an adjacent unstained section of the same lens on low emissivity glass used for infrared imaging. *C*, image shows the infrared signal map of the boxed region shown in *B* generated by collecting infrared spectra with a pixel resolution of 1.56 μm. *Green areas* are mineral regions and blue areas are protein regions. *D*, graphs show the spectra of a non-mineral region, two mineral regions, and the apatite standard. *Arrows* point to spectral features characteristic of apatite mineral. The scale bars in *A* and *B* represent 200 μm. The scale bars in the insets of panels *A* and *B* represent 52.5 μm and 41.5 μm, respectively.

The levels of γ-crystallins were different between heterozygous and homozygous *CrygC*^{dup} lenses. A decrease in levels of water-soluble γ-crystallins has also been reported in γD-V76D-crystallin mutant mouse lenses, although these authors found reductions in both heterozygotes and homozygotes (29), unlike our results in which decreased levels were only observed in *CrygC*^{dup} homozygotes. Because the γC-crystallin gene is activated at 11.5 dpc in the mouse lens (19) and the onset of primary fiber cell differentiation occurs at embryonic day 12.5, it is possible that the observed decreases in αA-, βB1- and γ-crystallins result from the *CrygC*^{dup}-induced impaired differentiation. The homozygous *CrygC*^{dup} lenses showed marked abnormalities of lens differentiation including impaired nuclear and organellar degradation (as shown by the persistence of nuclei and nuclear remnants and elevated levels of resident proteins of nuclei, ER, and Golgi). Impaired denucleation may be a common feature in γ-crystallin mutant lenses since it was also observed in mouse lines carrying mutations in several

different γ-crystallin family members (31, 32, 37). The homozygous *CrygC*^{dup} lenses also showed major alterations in fiber cell shape, size, orientation, and organization in the lens core (with little change in the organization of outer cortical fiber cells). These changes in cell arrangement resemble those described for the CRYGC p.(Leu160Stop) mouse lenses (33) and some of those reported for the *Crygc*^{Chl3} lenses that contain degenerated embryonic primary fiber cells and a distinct border between the lens core and the cortex (31). The presence of persistent organelles, nuclei, and nuclear remnants (in fiber cells that are normally free of these subcellular structures) and the disordered packing of fiber cells (due to changes in cell shape, size and orientation) would interfere with normal transparency and light transmission, contributing to light scattering. Thus, it is possible that the impaired organelle degradation and disordered packing of fiber cells contribute to the central cataract and the surrounding opacity in homozygous *CrygC*^{dup} lenses.

γ-crystallin mutations, connexins, and gap junction–mediated intercellular communication

Expression of the γC-crystallin mutant led to very reduced levels of Cx46 and Cx50 and major alterations in the abundance and distribution of gap junctions containing these proteins. Decreased levels of Cx46 and Cx50 have also been described in γD-V76D-crystallin mutant mouse lenses (29), suggesting that reductions in the lens fiber cell connexins might be a common alteration in mice carrying mutations of γC- or γD-crystallins (and perhaps other members of the γ-crystallin family). Because the decreases in levels of Cx46 and Cx50 proteins in heterozygous and homozygous *CrygC*^{dup} mice at 30 days of age were not paralleled by major changes in connexin mRNA levels, the results suggest that the connexin proteins are degraded in the mutant lenses. This interpretation is supported by the immunofluorescence data showing reductions of immunoreactive connexin-containing punctae. Considering that the reduction in fiber cell connexin levels was similar between heterozygous and homozygous *CrygC*^{dup} lenses, this alteration can only account for part of the much more pronounced decrease in fiber cell coupling in homozygous vs. heterozygous lenses. Most likely, the severe fiber cell disorganization within the nuclear region of homozygous (not evident in heterozygous) *CrygC*^{dup} lenses also contributes to the absence of gap junction-mediated intercellular communication in the mature fiber cells from homozygous *CrygC*^{dup} lenses.

Consequences of the γ-crystallin mutation on the lens circulation

Gap junction–mediated fiber cell-to-fiber cell coupling plays a pivotal role in the circulation of ions, water, and molecules throughout the lens (30). It is reduced in several cataract mouse models with mutations in different genes, including those encoding Cx46 and Cx50 (reviewed in (27)). In the lenses from mouse cataract models with reduced gap junction coupling and consequent alterations of the lens circulation, the gradients of ion concentrations and hydrostatic pressure are substantially affected (reviewed in (27)). This alteration in the lens circulation (which also affects the gradient of Ca^{2+} concentrations) results in the accumulation of Ca^{2+} toward the center of the lens to levels that can become high enough to cause precipitation of Ca^{2+} ions by interaction with the anions present in the tissue. In the homozygous *CrygC*^{dup} lenses, connexin levels were significantly reduced, gap junction plaques were extremely rare, and coupling was absent in the mature fibers; therefore, accumulation of calcium ions in the center of the lens was expected to be extremely high and to surpass the K_{sp} for several calcium salts. We confirmed our inference by the detection of Alizarin red-stained material in precipitated particles from homozygous *CrygC*^{dup} lens homogenates and in lens whole-mounts, and by Yasue staining of lens sections from homozygous animals. Notably, the X-ray-dense material detected by micro-CT and the Alizarin red-stained material in whole-mounts localized to the same lens region occupied by the cataracts in homozygous *CrygC*^{dup} lenses. These results are similar to the observations in homozygous Cx46fs380, Cx50D47A, and Cx46-null lenses (13–16). In addition, using ATR-μFTIR, we identified this material as calcium phosphate in the form of apatite, the same mineral found in the Cx46fs380 and Cx50D47A mutant lenses (16). Insoluble calcium-containing material has been previously reported in cataractous lenses from various species, including humans and rodents (7–15, 38). Calcium and phosphate have also been identified in some case reports of human cataracts (39–41), further suggesting pathological mineralization of the organ (16, 42).

The gap junctional coupling data from homozygous *CrygC*^{dup} lenses are similar to those from Cx46$^{-/-}$ lenses, which lack Cx46 and have normal levels of Cx50 (43), and those from homozygous Cx46fs380 and Cx50D47A lenses (15, 44), which have decreased levels of both Cx46 and Cx50 (45, 46). Although the homozygotes in these mouse models have similar changes in gap junctional coupling, there does not seem to be a strict correlation between this parameter and the cataract phenotypes. The cataract severity in the homozygous *CrygC*^{dup} lenses seems comparable to that of the denser cataracts in the Cx46$^{-/-}$ lenses and much more pronounced than the cataracts of homozygous Cx46fs380 and Cx50D47A mice (45–47). Also, the severity of the cataract phenotype does not correlate directly with the presence of remaining organelles in these mouse models, because homozygous Cx46$^{-/-}$ and Cx46fs380 lenses show normal denucleation (46, 47), whereas Cx50D47A lenses show impaired differentiation with remaining nuclei and nuclear fragments (45).

The data obtained from heterozygous mice provide additional insight regarding the complex relationships between lens gap junctional coupling and cataracts. The reductions in gap junctional coupling in heterozygous *CrygC*^{dup} lenses are relatively similar to that of heterozygous Cx50D47A lenses (15); however, at 1 month of age, heterozygous Cx50D47A lenses contain nuclear cataracts while heterozygous *CrygC*^{dup} lenses are transparent. In several other mouse cataract models decreases in lens fiber cell gap junctional conductance (resulting from a decrease in connexin levels or from redistribution of the connexin in the membrane) do not necessarily

result in overt cataracts. For example, lenses from heterozygous Cx46-or Cx50-null mice, which have half the levels of the targeted connexin and normal levels of the other lens fiber cell connexin, are transparent even though they have reduced gap junctional conductance (43, 48). Mice null for both tropomodulin and phakinin have a 50% decrease in gap junctional conductance, but they do not develop overt cataracts (49, 50). Even in heterozygous Cx46fs380 lenses (containing decreased levels of both Cx46 and Cx50 and values of gap junctional conductance similar to those in $CrygC^{+/dup}$ lenses) opacities are not detected until ≥ 4 months of age (46). The critical variable may be the absolute magnitude of the intracellular concentration of free Ca^{2+} resulting from impairment of the lens circulation. Indeed, an increase in the intracellular concentration of $Ca^{2+} > 1$ μM is a common finding in mouse models that develop cataracts (14, 15, 51, 52). This suggests that the timing of cataract appearance may relate to how long it took for the concentration of free intracellular calcium ions to reach that value following disruption of the lens circulation.

Mechanism of cataract formation

The results obtained in $CrygC^{dup}$ lenses provide evidence for a relationship between soluble γ-crystallin proteins, differentiation and connexin stability/function that affects lens homeostasis and transparency. Based on the results presented, we propose that early expression of the γC-crystallin mutant (and/or loss of the wild-type protein) affects the differentiation of primary fiber cells and their normal and regular packing, resulting in a reduced area of specialized appositional membranes for stabilization of Cx46 and Cx50 in gap junction plaques. This results in the degradation of the connexins and decreased gap junctional intercellular communication. As a result of the decrease in gap junctional conductance, the lens circulation of ions and water is disrupted. Calcium ions accumulate and precipitate as apatite. The combination of calcium precipitates, disorganization of fiber cells, and the presence of residual organelles all disrupt normal light transmission, leading to severe nuclear cataracts and the halo-like surrounding opacity between the cortical and the nuclear regions in homozygous $CrygC^{dup}$ lenses.

Identification of calcium precipitates in homozygous $CrygC^{dup}$ lenses expands the number of cataract models in which similar precipitates have been identified. These results together with previous reports demonstrating the presence of calcium-insoluble material in human cataracts imply that these precipitates represent a more common characteristic of cataracts than previously realized. They further support the involvement of mineralization of the lens as a component of cataractogenesis regardless of the initial inciting cause.

Experimental procedures

Animals

Wild-type C57BL/6J mice (# 000664) and homozygous mice reportedly carrying a γB-crystallin mutation (S11R), B6.A-$Crygb^{S11R}$/BocJ (# 003838) (17, 53), were obtained from the Jackson Laboratory. The mutation arose spontaneously in the A/J inbred strain at the Jackson Laboratory, and it was backcrossed to the C57BL/6J background. Male and female mice from the crystallin mutant strain or the C57BL/6J strain were mated to obtain homozygous litters or wild-type C57BL/6J mice, respectively. To obtain heterozygous litters, mice homozygous for the crystallin mutant were mated with wild-type C57BL/6J mice of the opposite sex. Then, heterozygous male and female mice were mated to obtain the littermates of all genotypes. The genotypes of these mice were initially determined by PCR using genomic DNA isolated from tail biopsies as a template, Phusion High-Fidelity DNA polymerase (Thermo Fisher Scientific), and the satellite marker D1Mit156 (forward: TCTGCTGCCACTTCTGAGAA; reverse: TGTG TGTCTATGGACATGGATG). The expected size bands are 112 bp for the mutant allele (because it arose spontaneously in the A/J background) and 143 bp for the wild-type allele (because of the extensive backcross to the C57BL/6J strain). However, the mice we received from the Jackson Laboratory did not carry the described γB-crystallin mutation. All animal procedures were approved by the University of Chicago Animal Care and Use Committee and followed its guidelines.

Polymerase chain reaction

DNA sequence spanning exons 1 and 2 of mouse γB-crystallin was amplified by PCR using Phusion High-Fidelity DNA polymerase (ThermoFisher Scientific), genomic DNA from homozygous crystallin mutant mice as the template, and the following set of primers: sense, GTGTGATTTCCTGTG-GAGGCAGCAGTC and antisense, TCTAAAAATTCAC-CACCACGTTCCTGAGAACTG. The 618 bp amplicon was purified using the QIAquick PCR Purification Kit (Qiagen) and sequenced at the DNA Sequencing Facility of the University of Chicago.

Whole genome sequencing

Genomic DNA was obtained from tail samples of three homozygous crystallin mutant mice and subjected to whole genome sequencing using the NovaSEQ6000 System (Illumina, Inc) at the Genomics Facility of the University of Chicago. The data were analyzed by the Center for Research Informatics of the University of Chicago. The sequences were aligned to the GRCm38 reference genome and calibration was performed using the known variant annotation from dbSNP for the genomic DNA from the A/J mouse strain. Then, variant calling and annotation of the identified variants was performed.

Light microscopy analysis

Lenses were observed using a Zeiss Stemi-2000C stereo microscope (Carl Zeiss) equipped with a halogen lighting system for transmitted illumination. Darkfield images were acquired with a Zeiss AxioCam digital camera using Zeiss AxioVision software (45, 46). All settings (*e.g.*, illumination intensity, magnification, and exposure time) were kept constant during the acquisition of the images for each animal group.

Immunoblotting

Lenses were homogenized in PBS (pH 7.4) containing 4 mM EDTA, 2 mM PMSF, and cOmplete EDTA-free protease inhibitor mixture (Roche Applied Science) at a concentration of 1 tablet/7 ml using a glass-glass homogenizer followed by sonication. Protein concentrations were determined in the total homogenates using the Bio-Rad Protein Assay Dye Reagent Concentrate based on the method of Bradford (54).

Aqueous soluble and insoluble fractions were prepared as previously performed (55). An aliquot (100 µl) of each lens homogenate was centrifuged at 14,000*g* for 20 min at 4 °C, and the supernatant (soluble fractions) was collected. The pellets were rinsed by resuspension in 100 µl of homogenization buffer and centrifuged again at 14,000*g* for 20 min at 4 °C. Each resulting supernatant was combined with the respective initial supernatant bringing the final volume to 200 µl. The pellets (insoluble fractions) were resuspended in 200 µl of SDS-loading buffer, a volume equal to that of the supernatant fraction. The soluble and insoluble fractions were stored at −80 °C until use.

Immunoblotting was performed as previously described (56). Briefly, whole lens homogenate aliquots containing equal amounts of proteins were loaded per lane. For the soluble and insoluble fractions, a volume equal to twice the aliquot of the corresponding lens homogenate was loaded per lane. Proteins were resolved on SDS-polyacrylamide gels and electrotransferred to Immobilon P (Millipore). Equivalence of loading and transfer was confirmed by Ponceau S staining of the membranes. Then, the membranes were incubated using previously characterized anti-Cx46 and anti-Cx50 antibodies (45, 57), or rabbit polyclonal anti-αA-and anti-αB-crystallin antibodies (Enzo Life Sciences), mouse monoclonal anti-βB1-crystallin (H-3) antibody and rabbit polyclonal anti-TOM20 antibodies (Santa Cruz Biotechnology), rabbit polyclonal anti-γ-crystallin antibodies (a kind gift of Dr Samuel Zigler), rabbit polyclonal anti-GRP78 BiP antibodies (Abcam), and rabbit monoclonal anti-histone H3 (D1H2) antibody (Cell Signaling Technology). Afterward, the membranes were incubated in horseradish peroxidase-conjugated goat anti-rabbit IgG antibodies or peroxidase-conjugated goat anti-mouse IgG antibodies (Jackson Immunoresearch). Binding of secondary antibodies was detected using Cytiva Amersham ECL Western Blotting Detection Reagents (Fisher Scientific). The immunoreactive bands from a minimum of three independent experiments were quantified by densitometry using Adobe Photoshop CS3 (Adobe Systems Inc.). The results are reported as relative values of the levels detected in wild-type lenses (considered as a 100%). Graphs were prepared using SigmaPlot version 10.0 (Systat Software).

Membrane staining

Lenses from 10-day old mouse lenses were dissected and fixed in 4% paraformaldehyde in PBS for 1 h. The lenses were then rinsed three times in PBS for 10 min each and transferred to 30% sucrose in PBS, after which they were stored at 4 °C until use. On the day of sectioning, lenses were embedded in Tissue-Tek optimum cutting temperature (O.C.T.) compound (Fisher Scientific) and flash-frozen in liquid nitrogen. Twenty-µm sections were obtained using a Microm HM 550 cryostat (Leica Biosystems) and immediately placed in PBS. Then, sections were incubated in blocking solution (5% normal goat serum, 1% Triton X-100 in PBS) for 1 h, followed by incubation in Oregon Green 488 Wheat Germ Agglutinin (W7024, ThermoFisher Scientific) and Draq5 Fluorescent Probe solution (ThermoFisher Scientific) for 15 min in blocking solution. The sections were then rinsed five times in PBS for 7 min each. Coverslips were mounted using 2% propyl gallate (Sigma-Aldrich) in PBS: glycerol (1:1). Confocal microscopy was performed in the Integrated Light Microscopy Core at the University of Chicago, which receives financial support from the Cancer Center Support Grant (P30CA014599). RRID: SCR_019197. Multiple images covering the lens center were acquired using a Leica SP5 STED (SP5 II) inverted laser scanning confocal microscope (Leica Microsystems) equipped with a 5 line argon laser at 458 nm, 476 nm, 488 nm, 496 nm, and 514 nm; DPSS laser at 561 nm; HeNe laser at 594 nm; HeNe laser at 633 nm. Sequential illumination with the appropriate wavelengths was used to avoid the bleeding of signals between channels. A seamless panoramic image of the lens center was generated using the Photomerge command of Adobe Photoshop 2022 (Adobe Systems Inc.).

Immunofluorescence

Immunofluorescence was performed as previously described (45). Nuclei were stained with Draq5 Fluorescent Probe solution (ThermoFisher Scientific) and filamentous actin was stained with Alexa Fluor 488 Phalloidin (ThermoFisher Scientific). Images were acquired using a Leica SP5 STED confocal microscope (Leica Microsystems) at the Light Microscopy Facility of the University of Chicago. Sequential illumination with the appropriate wavelengths was used to avoid the bleeding of signals between channels.

Reverse transcription real-time PCR

Lenses from 30-day-old mice of different genotypes were homogenized in QIAzol Lysis Reagent (Qiagen) using a glass-glass homogenizer, and the samples were processed for reverse transcription real-time PCR as described previously (56) using the following primers for mouse Cx50 (sense, TTTGACAGAGGTTGGAATGG and antisense, GCAGGGTTTCTTGGTAACTC), and for mouse Cx46 (sense, GTCACTGGTACTCAACATGC and antisense, CATCTGGGTTGAAGTGGTTAG). The transcript for cyclophilin A, a housekeeping gene, was used to normalize the relative levels of RNA among the different genotypes.

Electrophysiological measurements

Mice were sacrificed at 91–118 days of age by peritoneal injection of pentobarbital (100 mg/kg of weight), the eyes were removed, and the lenses were dissected in normal Tyrode's

solution (137.7 mM NaCl, 2.3 mM NaOH, 5.4 mM KCl, 2 mM $CaCl_2$, 1 mM $MgCl_2$, 5 mM HEPES, 10 mM glucose, pH 7.4). The series resistance between fiber cells was determined as previously described (44). The values obtained were curve fitted to the equivalent circuit model of the lens. Data are presented as mean ± S.E.M. All experiments were conducted on freshly dissected lenses.

Alizarin red staining of whole-mount lenses and their insoluble fractions

To stain insoluble material from the lenses, wild-type, heterozygous, and homozygous crystallin mutant lenses were homogenized in PBS containing cOmplete EDTA-free protease inhibitor cocktail (Roche Applied Science) at a concentration of 1 tablet/7 ml using a glass-glass homogenizer. The homogenates were centrifuged at 16,000*g* for 20 min, and the resulting pellet was resuspended in homogenization buffer. Equal amounts of the resuspended pellet and a filtered solution of 2% Alizarin red in water pH 4.1 to 4.3 were added to a glass slide and mixed by pipetting up and down as previously reported (16).

Lenses from wild-type and homozygous crystallin mutant animals were processed for whole-mount staining with Alizarin red as previously performed (14).

High-resolution micro-CT

After acquiring darkfield images, lenses were fixed in 5% paraformaldehyde in PBS for 48 h and scanned by high-resolution micro-CT to detect the presence or absence of high X-ray attenuating (mineralized) material using a Skyscan 1172 Micro CT System at 60 kV with a final image stack resolution of 3 to 6 μm cubic voxels. We examined a total of four wild-type and four homozygous crystallin mutant mouse lenses. The micro-CT scans were performed by an investigator who was unaware of the genotypes. Three-dimensional image stacks were viewed using ImageJ (as distributed through fiji.sc) (58). Movies from the three-dimensional scan stacks were generated using 3D Slicer (59).

Yasue staining

After micro-CT scanning, each lens was dehydrated, embedded in paraffin, and cut to obtain 5-μm sections. Alternating sections were deposited on regular glass for staining with the Yasue method to show calcium salts (60) and on low-emissivity (low-E) glass for infrared microspectroscopy.

Fourier-transform infrared microspectroscopy

The crystal composition of homozygous crystallin mutant lenses was determined by Attenuated Total Internal Reflection Fourier-transform infrared microspectroscopy (ATR-μFTIR). The unstained tissue sections were imaged using the visible CCD camera and frame grabber on the Spectrum Spotlight (61). Infrared images over the selected area were collected with a PerkinElmer Spotlight 400 infrared microscope interfaced to a PerkinElmer Frontier FTIR. The system employed a 16 × 1, liquid nitrogen–cooled, mercury cadmium telluride (HgCdTe) array detector. The ATR imaging accessory is based on a germanium internal reflection element which enables infrared spectra to be collected at a pixel resolution of 1.56 μm. Each spectrum in the image represents the average of four individual scans collected at a spectral resolution of eight wavenumbers (cm^{-1}).

Statistics

Data were analyzed for statistical significance using two-tailed Student's *t* test. A p value <0.05 was considered significant.

Data availability

All the relevant data are contained within the article and supporting information.

Supporting information—This article contains supporting information.

Author contributions—E. C. B. and V. M. B. conceptualization; P. J. M., J. G., J. C. W., S. B. B., A. J. S., and V. M. B. investigation; P. J. M., J. G., R. T. M., J. C. W., A. J. S., and V. M. B. formal analysis; P. J. M. and V. M. B. data curation; V. M. B. writing-original draft; P. J. M., J. G., R. T. M., J. C. W., S. B. B., A. J. S., E. C. B., and V. M. B. writing-review and editing; E. C. B. and V. M. B. supervision; J. C. W., E. C. B., and V. M. B. funding acquisition.

Funding and additional information—This work was supported by NIH grant R01-EY030914 (to E. C. B. and V. M. B.), and NIH grant S10 RR023710 (to J. C. W.). The content of this article is solely the responsibility of the authors and does not necessarily represent the official views of the National Institutes of Health.

Conflict of interest—The authors declare that they have no conflicts of interest with the contents of this article.

Abbreviations—The abbreviations used are: ATR-μFTIR, Attenuated Total Internal Reflection Fourier-transform infrared microspectroscopy; Cx46, connexin46; Cx50, connexin50; GRP78, 78 kDa glucose-regulated protein; micro-CT, micro-computed tomography; TOM20, translocase of outer mitochondrial membrane 20.

References

1. Horwitz, J. (2003) α-crystallin. *Exp. Eye Res.* **76**, 145–153
2. Bloemendal, H., de Jong, W., Jaenicke, R., Lubsen, N. H., Slingsby, C., and Tardieu, A. (2004) Ageing and vision: structure, stability and function of lens crystallins. *Prog. Biophys. Mol. Biol.* **86**, 407–485
3. Resnikoff, S., Pascolini, D., Etya'ale, D., Kocur, I., Pararajasegaram, R., Pokharel, G. P., *et al.* (2004) Global data on visual impairment in the year 2002. *Bull. World Health Organ.* **82**, 844–851
4. Sharma, K. K., and Santhoshkumar, P. (2009) Lens aging: Effects of crystallins. *Biochim. Biophys. Acta* **1790**, 1095–1108
5. Truscott, R. J. W., and Friedrich, M. G. (2019) Molecular processes implicated in human age-related nuclear cataract. *Invest. Ophthalmol. Vis. Sci.* **60**, 5007–5021
6. Shiels, A., Bennett, T. M., and Hejtmancik, J. F. (2010) *Cat-Map*: putting cataract on the map. *Mol. Vis.* **16**, 2007–2015

7. Jacob, A. (1851) *Cataract. Structure of the Lens and the Nature of its Opacity. On Cataract, and the Operation of its Removal by Absorption with the Fine Needle through the Cornea*. Medical Press Office, Dublin: 1–60
8. Zimmerman, L. E., and Johnson, F. B. (1958) Calcium oxalate crystals within ocular tissues. A clinicopathologic and histochemical study. *AMA Arch. Ophthalmol.* **60**, 372–383
9. Bron, A. J., and Habgood, J. O. (1976) Morgagnian cataract. *Trans. Ophthalmol. Soc. UK.* **96**, 265–277
10. Pau, H., and Förster, H. (1982) Double refraction of crystals in the lens (spheroliths, "Christmas tree ornaments") and in the vitreous body (scintillatio nivea). *Graefes Arch. Clin. Exp. Ophthalmol.* **219**, 295–297
11. Pau, H. (1984) Spheroliths in the lens. *Klin. Monbl. Augenheilkd.* **184**, 159–162
12. Antunes, A., Safatle, A. M., Barros, P. S., and Morelhão, S. L. (2006) X-ray imaging in advanced studies of ophthalmic diseases. *Med. Phys.* **33**, 2338–2343
13. Li, Y., Parkinson, D. Y., Feng, J., Xia, C.-h., and Gong, X. (2021) Quantitative X-ray tomographic analysis reveals calcium precipitation in cataractogenesis. *Sci. Rep.* **11**, 17401
14. Gao, J., Minogue, P. J., Beyer, E. C., Mathias, R. T., and Berthoud, V. M. (2018) Disruption of the lens circulation causes calcium accumulation and precipitates in connexin mutant mice. *Am. J. Physiol. Cell Physiol.* **314**, C492–C503
15. Berthoud, V. M., Gao, J., Minogue, P. J., Jara, O., Mathias, R. T., and Beyer, E. C. (2019) The connexin50D47A mutant causes cataracts by calcium precipitation. *Invest. Ophthalmol. Vis. Sci.* **60**, 2336–2346
16. Minogue, P. J., Sommer, A. J., Williams, J. C., Jr., Bledsoe, S. B., Beyer, E. C., and Berthoud, V. M. (2022) Connexin mutants cause cataracts through deposition of apatite. *Front. Cell Dev. Biol.* **10**, 951231
17. Li, L., Chang, B., Cheng, C., Chang, D., Hawes, N. L., Xia, C.-h., *et al.* (2008) Dense nuclear cataract caused by the γB-crystallin S11R point mutation. *Invest. Ophthalmol. Vis. Sci.* **49**, 304–309
18. Goring, D. R., Breitman, M. L., and Tsui, L. C. (1992) Temporal regulation of six crystallin transcripts during mouse lens development. *Exp. Eye Res.* **54**, 785–795
19. Nishiguchi, S., Wood, H., Kondoh, H., Lovell-Badge, R., and Episkopou, V. (1998) *Sox1* directly regulates the γ-crystallin genes and is essential for lens development in mice. *Genes Dev.* **12**, 776–781
20. Murer-Orlando, M., Paterson, R. C., Lok, S., Tsui, L.-C., and Breitman, M. L. (1987) Differential regulation of γ-crystallin genes during mouse lens development. *Dev. Biol.* **119**, 260–267
21. Ruotolo, R., Grassi, F., Percudani, R., Rivetti, C., Martorana, D., Maraini, G., *et al.* (2003) Gene expression profiling in human age-related nuclear cataract. *Mol. Vis.* **9**, 538–548
22. Wang, X., Garcia, C. M., Shui, Y. B., and Beebe, D. C. (2004) Expression and regulation of α-, β-, and γ-crystallins in mammalian lens epithelial cells. *Invest. Ophthalmol. Vis. Sci.* **45**, 3608–3619
23. Zhao, Y., Wilmarth, P. A., Cheng, C., Limi, S., Fowler, V. M., Zheng, D., *et al.* (2019) Proteome-transcriptome analysis and proteome remodeling in mouse lens epithelium and fibers. *Exp. Eye Res.* **179**, 32–46
24. Slingsby, C., and Clout, N. J. (1999) Structure of the crystallins. *Eye (Lond.).* **13**, 395–402
25. Vendra, V. P., Khan, I., Chandani, S., Muniyandi, A., and Balasubramanian, D. (2016) Gamma crystallins of the human eye lens. *Biochim. Biophys. Acta* **1860**, 333–343
26. Graw, J. (2004) Congenital hereditary cataracts. *Int. J. Dev. Biol.* **48**, 1031–1044
27. Beyer, E. C., Mathias, R. T., and Berthoud, V. M. (2022) Loss of fiber cell communication may contribute to the development of cataracts of many different etiologies. *Front. Physiol.* **13**, 989524
28. Liu, H., Du, X., Wang, M., Huang, Q., Ding, L., McDonald, H. W., *et al.* (2005) Crystallin γB-I4F mutant protein binds to α-crystallin and affects lens transparency. *J. Biol. Chem.* **280**, 25071–25078
29. Wang, K., Cheng, C., Li, L., Liu, H., Huang, Q., Xia, C.-h., *et al.* (2007) γD-crystallin–associated protein aggregation and lens fiber cell denucleation. *Invest. Ophthalmol. Vis. Sci.* **48**, 3719–3728
30. Mathias, R. T., Kistler, J., and Donaldson, P. (2007) The lens circulation. *J. Membr. Biol.* **216**, 1–16
31. Graw, J., Neuhäuser-Klaus, A., Löster, J., and Favor, J. (2002) A 6-bp deletion in the *Crygc* gene leading to a nuclear and radial cataract in the mouse. *Invest. Ophthalmol. Vis. Sci.* **43**, 236–240
32. Graw, J., Neuhäuser-Klaus, A., Klopp, N., Selby, P. B., Löster, J., and Favor, J. (2004) Genetic and allelic heterogeneity of *Cryg* mutations in eight distinct forms of dominant cataract in the mouse. *Invest. Ophthalmol. Vis. Sci.* **45**, 1202–1213
33. Zhao, L., Li, K., Bao, S., Zhou, Y., Liang, Y., Zhao, G., *et al.* (2010) A 1-bp deletion in the γC-crystallin leads to dominant cataracts in mice. *Mamm. Genome* **21**, 361–369
34. David, L. L., Azuma, M., and Shearer, T. R. (1994) Cataract and the acceleration of calpain-induced β-crystallin insolubilization occurring during normal maturation of rat lens. *Invest. Ophthalmol. Vis. Sci.* **35**, 785–793
35. Wang, Y., Lomakin, A., McManus, J. J., Ogun, O., and Benedek, G. B. (2010) Phase behavior of mixtures of human lens proteins Gamma D and Beta B1. *Proc. Natl. Acad. Sci. U. S. A.* **107**, 13282–13287
36. Serebryany, E., and King, J. A. (2014) The βγ-crystallins: Native state stability and pathways to aggregation. *Prog. Biophys. Mol. Biol.* **115**, 32–41
37. Graw, J., Löster, J., Soewarto, D., Fuchs, H., Reis, A., Wolf, E., *et al.* (2002) V76D mutation in a conserved γD-crystallin region leads to dominant cataracts in mice. *Mamm. Genome* **13**, 452–455
38. Zhou, Y., Bennett, T. M., and Shiels, A. (2021) Mutation of the TRPM3 cation channel underlies progressive cataract development and lens calcification associated with pro-fibrotic and immune cell responses. *FASEB J.* **35**, e21288
39. Fagerholm, P., Philipson, B., and Carlström, D. (1982) Calcification in the human lens. *Curr. Eye Res.* **1**, 629–633
40. Fagerholm, P., Lundevall, E., Trocmé, S., and Wroblewski, R. (1986) Human and experimental lens repair and calcification. *Exp. Eye Res.* **43**, 965–972
41. Chen, K.-H., Cheng, W.-T., Li, M.-J., Yang, D.-M., and Lin, S.-Y. (2005) Calcification of senile cataractous lens determined by Fourier transform infrared (FTIR) and Raman microspectroscopies. *J. Microsc.* **219**, 36–41
42. Berthoud, V. M., Gao, J., Minogue, P. J., Jara, O., Mathias, R. T., and Beyer, E. C. (2020) Connexin mutants compromise the lens circulation and cause cataracts through biomineralization. *Int. J. Mol. Sci.* **21**, 5822
43. Gong, X., Baldo, G. J., Kumar, N. M., Gilula, N. B., and Mathias, R. T. (1998) Gap junctional coupling in lenses lacking α_3 connexin. *Proc. Natl. Acad. Sci. U. S. A.* **95**, 15303–15308
44. Minogue, P. J., Gao, J., Zoltoski, R. K., Novak, L. A., Mathias, R. T., Beyer, E. C., *et al.* (2017) Physiological and optical alterations precede the appearance of cataracts in Cx46fs380 mice. *Invest. Ophthalmol. Vis. Sci.* **58**, 4366–4374
45. Berthoud, V. M., Minogue, P. J., Yu, H., Schroeder, R., Snabb, J. I., and Beyer, E. C. (2013) Connexin50D47A decreases levels of fiber cell connexins and impairs lens fiber cell differentiation. *Invest. Ophthalmol. Vis. Sci.* **54**, 7614–7622
46. Berthoud, V. M., Minogue, P. J., Yu, H., Snabb, J. I., and Beyer, E. C. (2014) Connexin46fs380 causes progressive cataracts. *Invest. Ophthalmol. Vis. Sci.* **55**, 6639–6648
47. Mathias, R. T., White, T. W., and Gong, X. (2010) Lens gap junctions in growth, differentiation, and homeostasis. *Physiol. Rev.* **90**, 179–206
48. Baldo, G. J., Gong, X., Martinez-Wittinghan, F. J., Kumar, N. M., Gilula, N. B., and Mathias, R. T. (2001) Gap junctional coupling in lenses from α_8 connexin knockout mice. *J. Gen. Physiol.* **118**, 447–456
49. Gokhin, D. S., Nowak, R. B., Kim, N. E., Arnett, E. E., Chen, A. C., Sah, R. L., *et al.* (2012) Tmod1 and CP49 synergize to control the fiber cell geometry, transparency, and mechanical stiffness of the mouse lens. *PLoS One* **7**, e48734

50. Cheng, C., Nowak, R. B., Gao, J., Sun, X., Biswas, S. K., Lo, W. K., *et al.* (2015) Lens ion homeostasis relies on the assembly and/or stability of large connexin 46 gap junction plaques on the broad sides of differentiating fiber cells. *Am. J. Physiol. Cell Physiol.* **308**, C835–C847
51. Gao, J., Sun, X., Martinez-Wittinghan, F. J., Gong, X., White, T. W., and Mathias, R. T. (2004) Connections between connexins, calcium, and cataracts in the lens. *J. Gen. Physiol.* **124**, 289–300
52. Liu, K., Lyu, L., Chin, D., Gao, J., Sun, X., Shang, F., *et al.* (2015) Altered ubiquitin causes perturbed calcium homeostasis, hyperactivation of calpain, dysregulated differentiation, and cataract. *Proc. Natl. Acad. Sci. U. S. A.* **112**, 1071–1076
53. Li, L., Cheng, C., Xia, C.-h., White, T. W., Fletcher, D. A., and Gong, X. (2010) Connexin mediated cataract prevention in mice. *PLoS One* **5**, e12624
54. Bradford, M. M. (1976) A rapid and sensitive method for the quantitation of microgram quantities of protein utilizing the principle of protein-dye binding. *Anal. Biochem.* **72**, 248–254
55. Chung, J., Berthoud, V. M., Novak, L., Zoltoski, R., Heilbrunn, B., Minogue, P. J., *et al.* (2007) Transgenic overexpression of connexin50 induces cataracts. *Exp. Eye Res.* **84**, 513–528
56. Berthoud, V. M., Minogue, P. J., Lambert, P. A., Snabb, J. I., and Beyer, E. C. (2016) The cataract-linked mutant connexin50D47A causes endoplasmic reticulum stress in mouse lenses. *J. Biol. Chem.* **291**, 17569–17578
57. Berthoud, V. M., Minogue, P. J., Guo, J., Williamson, E. K., Xu, X., Ebihara, L., *et al.* (2003) Loss of function and impaired degradation of a cataract-associated mutant connexin50. *Eur. J. Cell Biol.* **82**, 209–221
58. Schindelin, J., Arganda-Carreras, I., Frise, E., Kaynig, V., Longair, M., Pietzsch, T., *et al.* (2012) Fiji: an open-source platform for biological-image analysis. *Nat. Met.* **9**, 676–682
59. Fedorov, A., Beichel, R., Kalpathy-Cramer, J., Finet, J., Fillion-Robin, J.-C., Pujol, S., *et al.* (2012) 3D Slicer as an image computing platform for the Quantitative Imaging Network. *Magn. Reson. Imaging* **30**, 1323–1341
60. Yasue, T. (1969) Histochemical identification of calcium oxalate. *Acta Histochem. Cytochem.* **2**, 83–95
61. Gulley-Stahl, H. J., Bledsoe, S. B., Evan, A. P., and Sommer, A. J. (2010) The advantages of an attenuated total internal reflection infrared microspectroscopic imaging approach for kidney biopsy analysis. *App. Spectrosc.* **64**, 15–22